Department of Precision and Microsystems Engineering

Analysis and design of a sprung rotational energy harvester for wrist-worn wearables subject to a range of low frequency excitations

Sam van den Oever

Report no : 2023.028
Coach : Ir. W.W.P.J. van de Sande
Professor : Prof.dr.ir. J.L. Herder
Specialisation : Mechatronic System Design
Type of report : Master Thesis
Date : 11 May 2023

Analysis and design of a sprung rotational energy harvester for wrist-worn wearables subject to a range of low frequency excitations

MSc Thesis

Sam van den Oever

Delft University of Technology

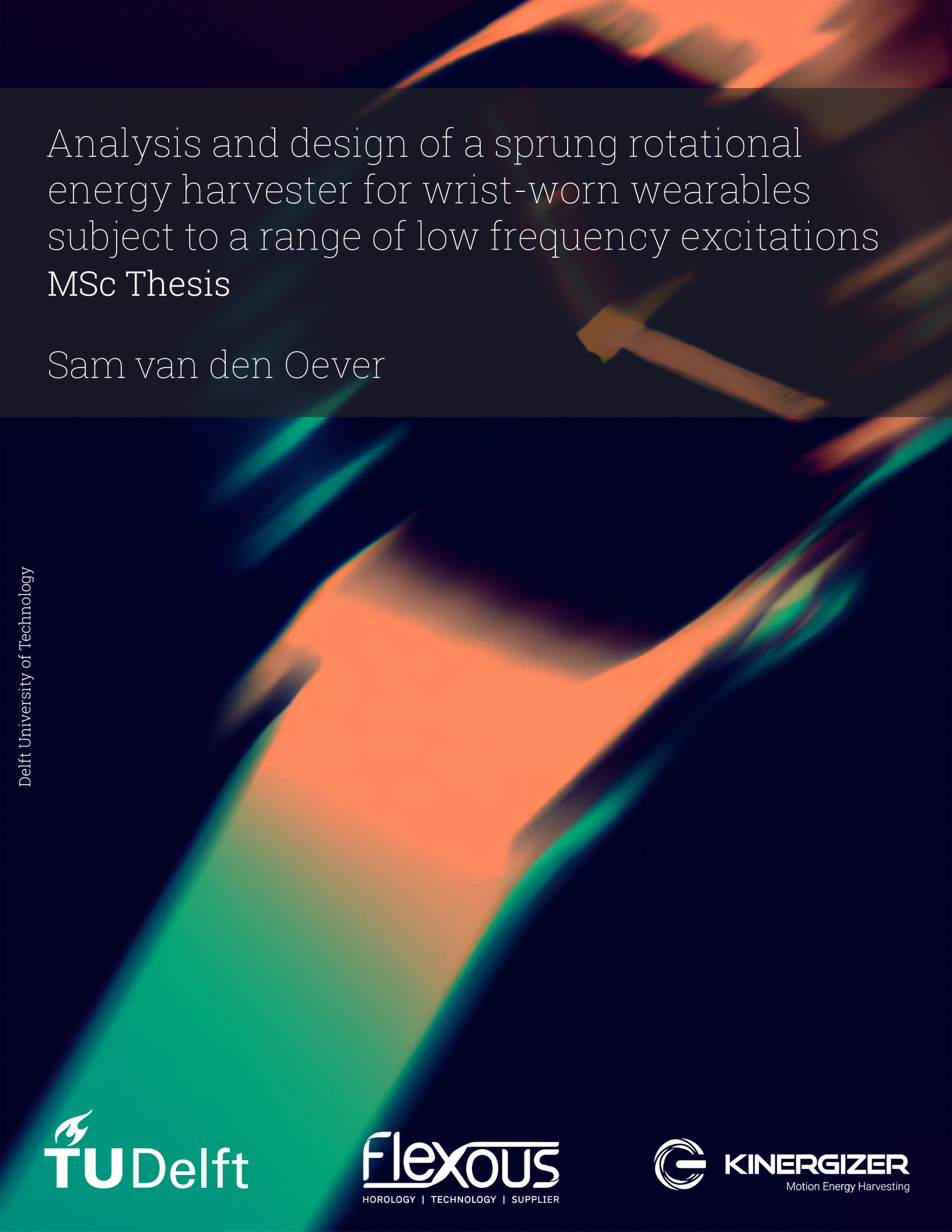

Analysis and design of a sprung rotational energy harvester for wrist-worn wearables subject to a range of low frequency excitations

by

S.J. van den Oever

to obtain the degree of Master of Science
at the Delft University of Technology
to be defended publicly on Thursday May 11, 2023 at 14:30 AM.

Student number:	4595653	
Thesis committee:	Prof. Dr. Ir. J. Herder,	TU Delft, chair
	Ir. W. van de Sande,	TU Delft, supervisor
	Dr. Ir. G. Radaelli,	TU Delft, external board member
	Dr. Ir. G. Dunning,	Flexous, supervisor

I. Preface

This thesis is the culmination of seven inspiring years in Delft, ending at the department of High-Tech Engineering. The conceptualization, research and writing that led to this thesis have taught me a lot about having trust in a process and individually creating and formulating solutions. The research that led to the paper presented in this thesis was commissioned by horology company Flexous and Kinergizer, who focus on ambient motion energy harvesting. Throughout the whole process of my research these companies have enabled me to prosper. Through providing a comfortable place to study literature, by offering tools and space for prototype production and testing and most importantly by valuing the work I have done. Experiencing the trust in my research leading to an internal follow-up investigation by Flexous gave me confidence in my capabilities as an engineer. I want to thank everyone at Flexous and Kinergizer for creating an enjoyable and stimulating workplace, especially Joep Meij and Gerard Dunning for their supervision and guidance. It was a great fortune to always be able to ask Joep, or anyone else from the company, for a quick spar if I was stuck on something or just wanted to have someone to explain something to. Furthermore I want to thank Werner van de Sande for his supervision and both him and Just Herder for their fruitful feedback. I want to thank my dear friends and family for checking in on me every once in a while and lastly I want to thank Zola for her continuous support and confidence.

My interest in the field of compliant mechanisms sparked an enthusiastic start of the research in which a seemingly implausible initial research objective was formulated: The design of a continuously rotating compliant joint to facilitate movement of a rotational energy harvester found in watches. A literature review (appended in this thesis) gave insight into the possibilities and limitations of compliant joints and led to a new research question: How does the stiffness of a compliant mechanism influence a rotational energy harvester and how can it be used advantageously? The research paper presented in this thesis aims to answer this question. A design, prototype and test are presented for a sprung rotational energy harvester for wrist worn wearables subject to the low frequency excitations imposed by walking.

Sam van den Oever
Delft, April 2023

CONTENTS

Analysis and design of a sprung rotational energy harvester for wrist-worn wearables subject to a range of low frequency excitations

Sam van den Oever

***Abstract*—A growing energy demand has sparked interest into harvesting energy from the human body. Often, a rotational proof mass is used to harness energy for a wearable from kinetic motion of its user. The addition of a spring has the potential to significantly increase efficiency for these low-power rotational energy harvesters. In this research a system characterisation is performed from which a dimensionless ratio is formulated to determine optimal spring stiffness for maximisation of average power output as a function of harvester design parameters and excitation inputs. Creating a system that is optimized for the entirety of its operational range rather than for one specific excitation input. Implementation is investigated in the field of horology, where rotational energy harvesters are widely implemented. To increase harvesting efficiency of existing rotational energy harvesters without requiring significant design alterations a compliant design is proposed, prototyped and tested.**

***Keywords*—Sprung Rotational Energy Harvesting, Wearables, Watches, Compliant Mechanisms**

II. Introduction

Harvesting energy from sources presented by the world around us has been done for many years and is still one of the most developing fields of technological research [1]. While wind and the sun are well known sources of energy, recent research has shown people looking to themselves to power their technology. At the scale of wearable devices the interest in energy harvesting from the human body within a device is gaining a lot of attention [2, 3]. Although energy harvesting from the human body is a hot topic the principle is not new, automatic winding found in mechanical watches dates back to the 18th century. However, with the increasing amount of electronic wearables the ambition to generate electricity from human movement has sparked research into more efficient harvesting solutions and small scale transducers [4]. In low-power wireless electronic devices this could result in the replacement of batteries with small scale generators, evading pollution from disposable batteries and the need to recharge or replace them. Only a few finished products are found that harvest energy from the body to generate electricity, e.g. the Seiko Kinetic watch and the ETA autoquartz watch. However, many novel strategies have been proposed on how to incorporate an energy harvester into a small scale electronic device [5, 6, 7, 8, 9]. These designs often rely on the principle of using the inertia of a proof mass to create a motion input for an electrical transducer. Most of these 'kinetic energy harvesters' found in literature implement a rotating proof mass, further denoted as 'rotor', for harvesting from translation as well as rotation, while eliminating movement limitations due to a physical stop [10]. An in-depth review on these so called 'rotational energy harvesters' was performed by Fu et al. [11]. A strategy to increase harvesting potential of a rotational energy harvester is by introducing a stiffness to the rotor mechanism [10, 12]. Yeatman et al. derived the potential of a rotational energy harvester designed to resonate with the addition of a spring which Halim et al. [13] incorporated in the design of a novel transducer for electronic wearables under pseudo-walking excitation. For this harvester an optimal spring stiffness at a specific excitation input was determined, showing significantly increased harvesting potential. However, walking contains a large range of possible excitations at which energy can be harvested [14]. For sprung rotational harvesters that are subjected to a range of excitations, the duration and intensity of these excitations should influence the choice for an implemented stiffness. Optimizing for total power harvested throughout the day rather than instantaneous power at one excitation.

In this paper a method for the characterisation and design of a sprung rotational harvester subject to a range of excitation inputs is proposed. A ratio between spring stiffness and design parameters is defined and the effect of changing this ratio is discussed. This insight is aimed to create the possibility of designing a suitable sprung rotational energy harvester for any arbitrary use case with corresponding excitation inputs. A performance metric is proposed which is based on all excitations present in walking throughout the day and will be denoted as 'daily average power'. The rotational energy harvesting system found in the Seiko Kinetic watch, which is investigated by Xue et al. [15], is used as an example case to optimize for harvested power. A flexure mechanism was designed, prototyped and tested to be able to implement a stiffness into existing rotational energy harvesters without requiring major design changes. The design of this flexure mechanism was inspired by compliant joint designs discussed by Machekposhti et al. [16], specifically the large-stroke compliant joint proposed by Yu et al. [17]. Compliant mechanisms rely on bending to obtain complex functionality while negating friction and wear from interacting surfaces. Furthermore, compliant designs are tunable through shape and material choice allowing them to be more precise, lighter and more durable than their conventional counterparts [18], all of which are characteristics desired in wearables.

Several approaches were taken to analyse the system dynamics of a sprung rotational harvester subject to a range of excitations: the system was characterised by setting up the equation of motion (Ch. III-A), the system was simulated using a multi-body simulation tool (Ch. III-G) and finally a semi-compliant prototype was designed (Ch. III-H), prototyped and tested (Ch. III-I). The results can found in chapter IV and are discussed in chapter V.

III. Method

A. System characterisation

To characterise a sprung rotational energy harvester, a 2D model was created. The model is comprised of a sprung inverted pendulum where a torsional spring introduces a rotational stiffness to the rotational point of the pendulum and is in equilibrium when the pendulum is in the upright position. A representation of the system can be found in Fig. 1, where the model is shown in a deformed state. The dotted black line indicates the equilibrium position of the rotor and the dashed red line indicates an arbitrary but known path over which the rotational point of the rotor travels. The displacement of the rotational point of the rotor is denoted by X in the x-direction and Y in the y-direction. Note that, when in equilibrium, the spring suspends the rotor upwards against the direction of gravity. Creating a system which is thought to have increase harvesting potential with respect to an unsprung system by utilizing the direction of gravitational force to induce movement [13][19]. In similar fashion as an inverted pendulum, for which the instability of the mass gives the system a tendency to move under the effect of gravity as a result of only a slight perturbation.

In the following section the equation of motion for the proposed system is derived using the Lagrangian method. Note that the equation of motion of a similar system was derived by Rantz et al. [19]. Unlike in Rantz's study, Coulomb damping torque is added in the following section because it is thought to have a significant effect on the dynamics of the system [13, 15]. Because the path on which the rotational point of the pendulum travels is assumed to be known, the system is described by a single generalised coordinate: the relative angle of the rotor θ. A list of all relevant variables can be found in Tab. I. The Lagrangian of the system is defined by

$$L = K - V \tag{1}$$

[20], where K denotes the system's kinetic energy and V denotes the system's potential energy. To determine the kinetic and potential energy of the rotor the location of its centre of mass is determined. The position along the x-axis is defined as

$$r_x = X + lsin(\theta) \tag{2}$$

and along the y-axis as

$$r_y = Y + lcos(\theta), \tag{3}$$

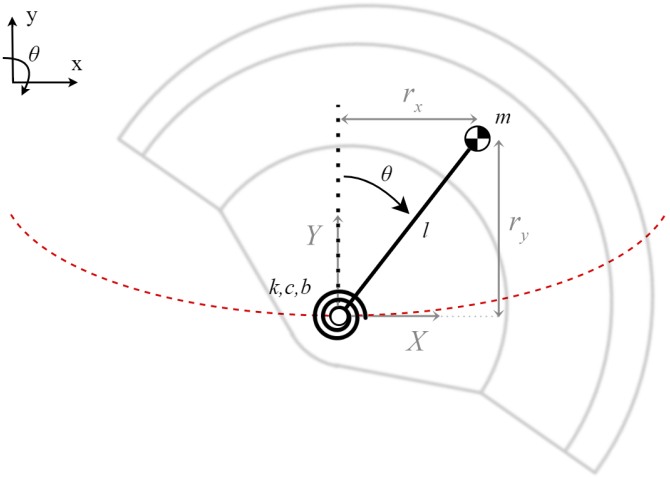

Fig. 1: Representation of the 2D model of a sprung rotational harvester. The rotor at angle θ from its equilibrium position follows an arbitrary path depicted by the dashed red line. The rotor is defined by it's mass m at eccentric length l from its rotational point. Which is subjected to friction, damping and torsional stiffness. Movement of the rotational point of the rotor is denoted by X and Y and displacement of its centre of mass is denoted by r_x and r_y.

as shown in Fig. 1. The velocity of the centre of mass can be obtained by differentiating the position with respect to time. Obtaining

$$v_x = \frac{d}{dt} r_x = \dot{X} + l\dot{\theta}cos(\theta) \tag{4}$$

and

$$v_y = \frac{d}{dt} r_y = \dot{Y} - l\dot{\theta}sin(\theta). \tag{5}$$

The resultant velocity is obtained by

$$v = \sqrt{v_x^2 + v_y^2}. \tag{6}$$

Movement of the centre of mass of the rotor is comprised of a translation and a rotation. Energy from translation of the centre of mass is defined by $\frac{1}{2}mv^2$ where v is determined from x and y displacements of the centre of mass as shown in Eq. 6. The angular rotation at the base of the rotor can be superimposed to obtain the rotation of its centre of mass, resulting in a rotational kinetic energy of $\frac{1}{2}I_g\dot{\theta}^2$. Total kinetic energy of the rotor becomes

$$K = \frac{1}{2}mv^2 + \frac{1}{2}I_g\dot{\theta}^2. \tag{7}$$

The potential energy of the system has a contribution from gravity and the torsional spring. Where gravitational potential increases with increasing r_y and is defined by $mg(l+r_y)$. Note

Variable	Defenition
θ	Relative rotor angle [rad]
θ_e	Relative rotor equilibrium angle [rad]
k	Torsional spring stiffness [Nm/rad]
m	Rotor mass [kg]
l	Eccentric rotor length [m]
c	Total viscous damping [Nms/rad]
c_e	Electrical damping
c_m	Mechanical damping
b	Coulomb damping torque [Nm]
I_g	Moment of inertia about centre of gravity [kgm^2]
I_r	Moment of inertia about axis of rotation [kgm^2]
ϕ	Input amplitude
f	Input frequency [s^{-1}]
L	Arm length [m]
P_{avg}	Average power [μW]
T	Harvesting period [s]

TABLE I: System variables

that the gravitational potential is zero when the rotor is in the downward position with respect to gravity, where $r_y = -l$. Energy in the spring increases with increasing rotor angle θ and is defined by $\frac{1}{2}k\theta^2$. The definition of potential energy becomes

$$V = mg(l + r_y) + \frac{1}{2}k\theta^2. \tag{8}$$

The Euler-Lagrange equation gives us the following relation [21]:

$$\frac{d}{dt}\frac{\delta L}{\delta \dot{\theta}} = \frac{\delta L}{\delta \theta} - \frac{\delta D}{\delta \dot{\theta}} \tag{9}$$

where resistive forces in the system are treated as a generalised force and are defined as the negative angular velocity gradient of a dissipation function D that includes both viscous and coulomb damping:

$$D = b\dot{\theta} + \frac{1}{2}c\dot{\theta}^2. \tag{10}$$

With coulomb damping torque b and viscous damping coefficient c. Substituting all equations and solving for angular acceleration $\ddot{\theta}$ yields the equation of motion of the system

$$\ddot{\theta} = -\frac{b + k\theta + c\dot{\theta} + ml(\ddot{X}cos(\theta) - \ddot{Y}sin(\theta) - gsin(\theta))}{ml^2 + I_g}. \tag{11}$$

The equation of motion is the same for an unsprung rotor mechanism where $k = 0$. To be able to compare the effect of different system parameters a performance metric is to be formulated. For this, two choices can be made. For systems that store energy mechanically, e.g a mechanical wristwatch, the harvested potential is directly related to the angular displacement of the rotor. A performance metric for these systems is formulated as the total travelled angle over the harvesting period. For electrical systems electromagnetic transduction is often used to convert kinetic energy to electric potential [11]. For these systems average power P_{avg} is a suitable performance metric which is dependent on angular velocity and electrical damping. The optimal generator configuration for energy harvesting in wearables is discussed by Xue et al. [22] and will not be a topic in this paper. For a harvesting period T, average power is denoted as [13]:

$$P_{avg} = \frac{1}{T}\int_0^T \frac{1}{2}c_e\dot{\theta}^2 dt. \tag{12}$$

B. Potential energy profile

The influence of a stiffness on the dynamics of a rotor is characterised by setting up the potential energy curves for various stiffnesses, found in Fig. 2. With these curves the equilibrium points of the system and their stability is visualised. The equilibrium points are found where the potential energy's

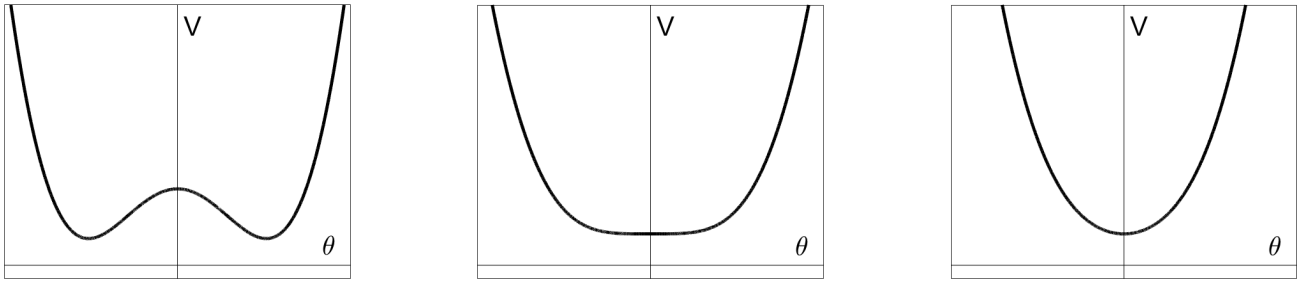

(a) $\alpha < 1$. (b) $\alpha = 1$. (c) $\alpha > 1$.

Fig. 2: Potential energy curves of a sprung rotor for different values of α.

derivative equals zero. Differentiating Eq. (8) with respect to rotor angle yields

$$\frac{dV}{d\theta} = -mglsin(\theta) + k\theta. \tag{13}$$

Setting the potential derivative to zero and separating angle and design parameters yields a dimensionless relation which will be denoted as α.

$$\frac{sin(\theta_e)}{\theta_e} = \frac{k}{mgl} = \alpha. \tag{14}$$

Where θ_e denotes the angle where the rotor is in equilibrium. Note that α has a linear dependence on spring stiffness k. While parameters like mass m and eccentric length l are often defined by bounds in the design space, spring stiffness is considered to be a design parameter which is more tunable within a realistic design space. The influence of α on the potential energy is visualised using potential energy diagrams shown in in Fig. 2a, Fig. 2b and Fig. 2c, considering the cases $\alpha < 1$, $\alpha = 1$ and $\alpha > 1$ respectively. In the case where $\alpha < 1$ a bi-stable system is created with two stable equilibria, corresponding to the rotor hanging to either side of the upright rotor position. For $\alpha > 1$ one stable equilibrium is observed, corresponding to the rotor being held in the upright position by the spring. In the special case where $\alpha = 1$ a plateau is observed which corresponds to an area where spring- and gravitational potential are almost equal and, over a limited range of motion, the system becomes 'energy-free' as proposed by Herder et al. [23].

C. Eccentric length

The mass moment of inertia of the rotor about it's rotational axis is defined by

$$I_r = m \cdot l^2. \tag{15}$$

Furthermore, the torque exerted by the rotor mass m about its rotational point is defined by

$$\tau = I_r \cdot \ddot{\theta}. \tag{16}$$

The torque exerted by the rotor should be high enough to overcome torque due to damping and friction in the system. The influence of eccentric length of the rotor on average power per excitation input was simulated by varying the eccentric length of an existing harvester mechanism while keeping mass m and α constant. From this, an insight was obtained of the effect of a rotor with a relatively small eccentric length, as seen in the design proposed by Halim et al. [13], and a relatively large eccentric length as seen in the rotational harvester in the Seiko Kinetic watch. In this research parameters of the Seiko Kinetic watch are used (Tab. III) to analyse this effect for an actual harvester. Note that, according to Eq. (14), only the spring stiffness changes with varying eccentric length when α and mass m are kept constant.

D. Excitation input

The excitation input defines the X and Y position of the base of the rotor. A repetitive motion can be described by an amplitude and frequency along a path defined by the geometry of the 'host' from which energy is to be harvested. The harvesters' optimal design parameters depend on the nature of the activities to which the system is subjected and from which energy is to be harvested. With α decreasing, the range of motion of the rotor increases when subjected to the same input energy, as can be observed in the difference in range of rotor angle θ between Fig. 2a, Fig. 2b and Fig. 2c. Because harvested potential is assumed to increase with range of motion of the rotor [11], the value of α has to be minimized. Note that, for the bi-stable system at $\alpha < 1$, the available energy from excitation input should be high enough for the rotor to overcome the potential peak to move from one equilibrium position to the other. This movement from one equilibrium position to the other will be called the 'flipping behaviour' of the rotor. The lowest possible value of α is determined by the lowest excitation input energy. The energy required to flip the rotor should not be higher than the available energy introduced by the lowest excitation input energy. The energy required to induce a flipping behaviour can be denoted as

$$E_f = E_p - E_{se} + W_r, \tag{17}$$

where E_p denotes the potential energy at the peak ($\theta = 0$), E_{se} denotes the potential energy at a stable equilibrium ($\theta = \pm\theta_e$) and W_r denotes the work by resistive forces from friction and damping. By plugging the corresponding angles into Eq. (8) the relation for E_f is found:

$$E_f = mgl(1 - cos(\theta_e)) - \frac{1}{2}k\theta_e^2 + W_r. \tag{18}$$

Rewriting Eq. (14) for k and plugging k into Eq. (18) yields

$$E_f = mgl(1 - cos(\theta_e)) - \frac{1}{2}mglsin(\theta_e)\theta_e + W_r. \tag{19}$$

When available energy E_i from the initial excitation input is known, α can be found by setting E_f equal to E_i, solving for θ_e and plugging into Eq. (14). Note that, for the case where $E_i < W_r$ at $\alpha \approx 1$, the rotor will not be able to flip at the initial excitation input due to friction and damping in the system.

In the case of a wrist-worn wearable subject to walking, the path travelled by the harvester can be approximated by a harmonic sine wave creating a 'pseudo-walking' movement as proposed by Halim et al. [13]. This path is defined by arm swing frequency, arm swing amplitude and arm length and is denoted as

$$X(t) = Lsin((\phi)sin(2\pi ft)) \tag{20}$$

and

$$Y(t) = L - Lcos((\phi)sin(2\pi ft)), \tag{21}$$

where L denotes arm length, ϕ denotes arm swing amplitude, f denotes arm swing frequency and t denotes time.

E. Walking

Walking contains a range of possible input combinations in terms of amplitude and frequency where the speed at which people walk affects the amplitude of a person's arm swing angle. Ford et al. [14] analysed the arm swing amplitude of ten healthy adults when walking at speeds ranging from 0.8 to 4.7 km/h. Data interpreted from this study can be found in Fig. 3. In this figure a distinction is made between walking slow and walking fast denoted by a red and blue area. Arm swing frequency was found to have a smaller variable range around a low frequency excitation of 1 Hz [24] and, for simulation, was simplified to three input cases at 0.9, 1.0 and 1.1 Hz. Covering the majority of arm swing frequencies found in walking. Johansson et al. [25] studied the daily activities of 1670 adults giving an insight into the average time spend walking per day and the ratio between walking slow (between 0.8 and $3km/h$) and walking fast (between 3 and $5km/h$). Accelerometers worn on the wrist for seven consecutive days were used to quantify minutes spend in different activities per day. Time spend walking slow, walking fast and running are shown in Tab. II. Note that, while time spend walking slow and time spend walking fast are in the same order of magnitude, minutes per day spend running was found to be significantly less and inconsistent for the average adult. Therefore, running was not considered as an excitation input for which to optimise in this research. Furthermore, the travelled path of the wrist during running varies from person to person and can not be described by Eq. (20) and (21).

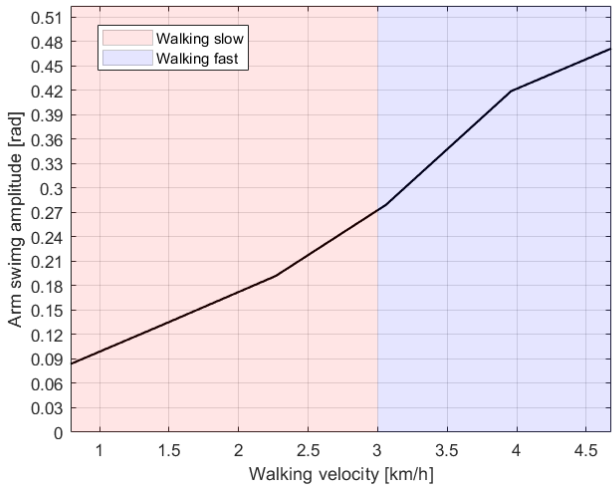

Fig. 3: Arm swing amplitude per walking velocity [14].

Activity	Median time spend [min/day]
Walking slow	19.48
Walking fast	55.07
Running	0.12

TABLE II: Time spend in physical activity per day [25].

F. Performance metric

By combining data on daily time spend per walking speed with average harvested power per arm swing input (P_{avg} from Eq. 24) an estimation can be made of average power harvested from walking throughout the whole day. This will be denoted as 'daily average power' (P_{da}) and used as a performance metric to compare between sprung and unsprung harvesters. This metric is calculated by taking the mean of the average powers of excitation inputs within an activity range and multiplying it by the minutes per day spend in that activity over the total minutes per day spend in the considered activities combined. For a harvester subjected to walking P_{da} is denoted as:

$$P_{da} = P_{avg.slow} \cdot \frac{19.48}{(19.48 + 55.07)} + P_{avg.fast} \cdot \frac{55.07}{(19.48 + 55.07)}. \tag{22}$$

$P_{avg.slow}$ denotes the mean of the average powers per excitation inputs considered as walking slow. $P_{avg.fast}$ denotes the mean of the average powers per excitation inputs considered as walking fast. The simplification is made that power is only harvested through walking. This is done to be able to define a performance metric for which simulations and a feasible physical test can be made. While walking is considered to be the main source of kinetic energy throughout the day, actual power production will be higher through all various activities performed when wearing a wrist-worn device.

G. Multibody simulation

To analyse the dynamics of the system a model was created using Simulink's Simscape Multibody tool. A pseudo walking model was set up in which a straight 0.57 m arm is actuated in a sinusoidal, pendulum-like swing. On the end of the arm a rotor is attached with a customizable shape, density, stiffness and damping. The model calculates and solves the

Parameter	Value	Unit
Rotor mass, m	$4.66 \cdot 10^{-3}$	kg
Eccentric rotor length, l	$4.00 \cdot 10^{-3}$	m
Total viscous damping, c	$5.30 \cdot 10^{-7}$	Nms/rad
Electrical damping, c_e	$4.00 \cdot 10^{-7}$	Nms/rad
Coulomb damping torque, b	$2.20 \cdot 10^{-5}$	Nm
Rotor mass moment of inertia, I_g	$2.50 \cdot 10^{-7}$	kgm^2
Arm length, L	$6.00 \cdot 10^{-1}$	m
Simulation length, T	30.0	s

TABLE III: Parameters of the Seiko Kinetic [15].

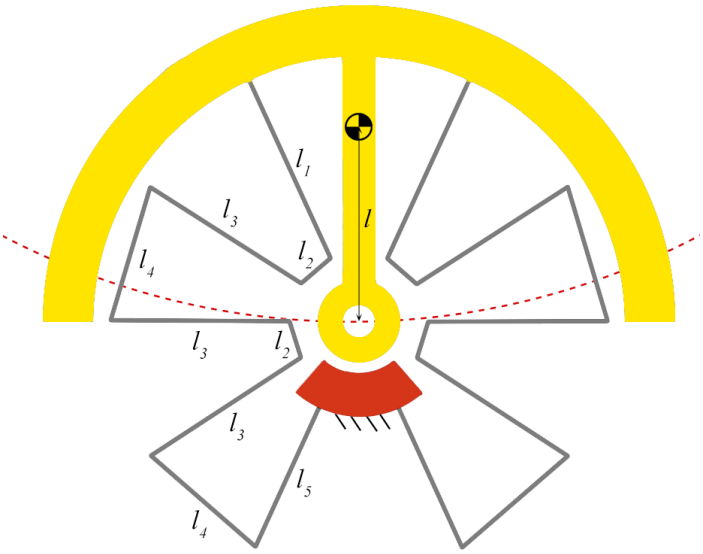

Fig. 4: Design of the flexure mechanism in the rotor plane where the rotor is shown in yellow and the ground connected to the harvester base is shown in orange. Flexures are shown in grey with corresponding lengths l_1-l_5. The centre of mass is located at length l from the centre of rotation. A pseudo-walking arm swing is denoted with a dashed red line.

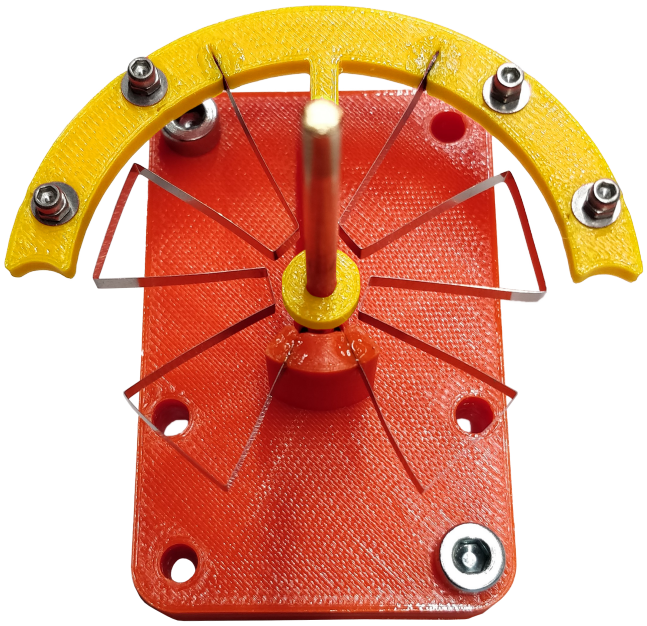

Fig. 5: Detailed picture of the manufactured prototype flexure mechanism. The rotor, shown in yellow, is press-fit onto a axle which is suspendend by a bearing in the orange backplate. A mount is incorporated in the orange backplate in which the bend flexure is glued. The other end of the flexures is glued into the rotor.

equations of motion from inserted geometries, parameter values and excitation input and gives the angular rotation of the rotor over time as output. Arm swing amplitude was swept over the range shown in Fig. 3 at 0.9, 1.0 and 1.1 Hz arm swing frequency. Simulations were performed for both sprung and unsprung ($k = 0$) rotational harvesters for which average power was calculated by plugging the angular velocity from angular displacement per simulation time step and the electrical damping of the simulated transducer into Eq. (12). Results discussed in the following section are from a pseudo-walking simulation with motion input according to Eq. (20) and (21) for wrist worn energy harvesters modeled as shown in Fig 1. The rotor specifications of the Seiko Kinetic watch were used to define rotor shape, weight and damping. Through the implementation of actual harvester parameters this research aims to obtain obtain realistic results for existing harvesters. The parameters of the Seiko Kinetic watch were obtained by Xue et al. [15] and are shown in Tab. III. Simulations were performed of daily average power for different stiffnesses, resulting in a range of values of α (0.6 to 1.5) to understand its influence on the harvesting potential of the system.

H. Flexure mechanism

The main challenge of creating a sprung rotational energy harvester is how to implement a rotational stiffness without requiring significant design alterations for existing harvester designs. A spiral spring is not desirable as it would intersect with the connection of the rotor to its rotational bearing, prohibiting it to be in the same plane as the rotor. A design was made that incorporates a leaf flexure in the plane of the rotor, in which space is evidently present to allow for rotation of the rotor. The flexure design, shown in Fig. 4, is comprised of two separate folded leaf flexures, shown in grey, that are connected to the ground of the harvester, shown in orange, on one end and to the rotor, shown in yellow, on the other end. By folding one metal strip effectively a system of

Parameter	**Value**	**Unit**
Length 1, l_1	$1.85 \cdot 10^{-2}$	m
Length 2, l_2	$3.65 \cdot 10^{-3}$	m
Length 3, l_3	$1.70 \cdot 10^{-2}$	m
Length 4, l_4	$1.32 \cdot 10^{-2}$	m
Length 5, l_5	$1.45 \cdot 10^{-2}$	m
Flexure thickness, t	$5.00 \cdot 10^{-5}$	m
Flexure width, w	$2.70 \cdot 10^{-3}$	m
Young's modulus, E	$1.95 \cdot 10^{11}$	N/m^2
Poisson's ratio, ν	$2.90 \cdot 10^{-1}$	-

TABLE IV: Flexure design parameters

multiple leaf flexures in series is created. The flexures were designed to be either perpendicular to- or in line with the axis through the center of rotation of the rotor. Length and thickness of the flexures in line with the center of rotation determine the stiffness of the mechanism, they are shown in Tab. IV together with the other design parameters. The flexure elements perpendicular to the center of rotation function as intermediate bodies to transfer force from flexure to flexure, in similar fashion as the mechanism proposed by Yu et al. [17]. It is important to note that the flexure mechanism was designed for torsional stiffness in the plane of the rotor. The flexure mechanism does not have to account for out-of-plane forces due to a separate bearing constraining the rotor in all degrees of freedom except rotation. Stiffness of the flexure design was analysed by performing a finite element method (FEM) analysis using the simulation software Ansys after which the flexure was produced by bending a single strip of 1.4310 stainless steel. The flexure elements were glued into the mount connected to the arm on one side and the rotor on the other side. The prototype can be seen in Fig. 5. After manufacturing a quasi-static analysis was performed where torque per radian of deflection was mapped over a constant low velocity of $8.6 \cdot 10^{-3} \frac{rad}{s}$ using a rheometer. From this, the stiffness of the mechanism was derived. The leaf flexure mechanism introduces a physical stop to the system, occurring when the spring is folded against its ground. Simulations were performed to analyse the influence of a physical stop on the harvested power of the system.

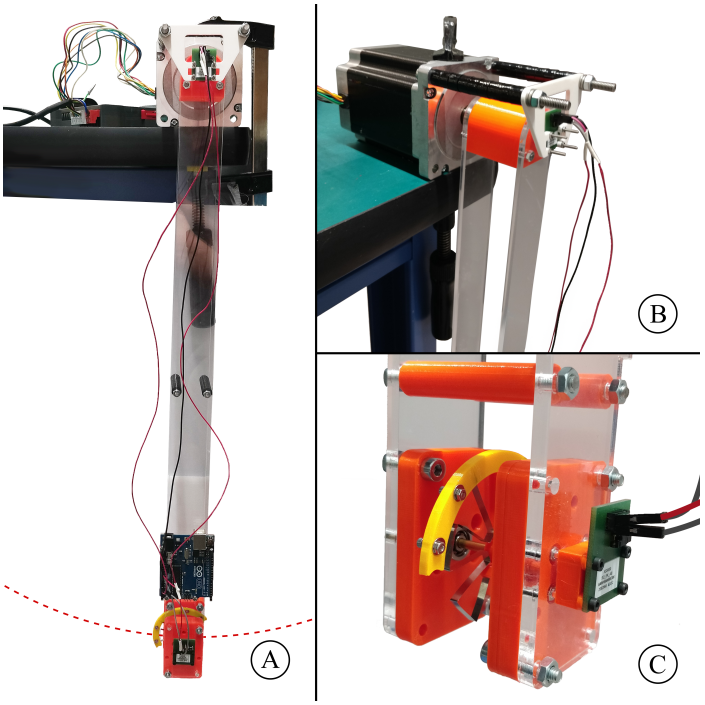

Fig. 6: (A) An overview of the pseudo walking test set-up, with travelled path denoted by a dashed red line, (B) Detailed depiction of the actuator with encoder, (C) Detailed depiction of the sprung harvester mechanism with encoder.

I. Test set-up

A physical test set-up was created to validate the working principle of the proposed flexure mechanism and to validate the proposed simulation model. To enable manufacturing of the prototype flexure mechanism within the scope of this research the dimensions of the rotor were scaled up with respect to rotors found in conventional rotational energy harvesters. Yielding a new eccentric length, mass and damping. An overview of the test set-up can be found in Fig. 6(A) together with a more detailed depiction of the actuator in Fig. 6(B) and the flexure mechanism and rotor in Fig. 6(C), both with corresponding encoder. A laser-cut acrylic arm was actuated using a NEMA 34 stepper motor enabling a rotational motion controlled by an Arduino UNO. On the end of the arm an axle with a rotor was suspended by two rotational ball bearings. The angular displacement of the rotor axle and the arm were measured using two ams AS5600 magnetic rotatry position sensors read out by a second Arduino UNO. Data from these sensors was used to obtain angular position and velocity data of the rotor axle and actual arm swing amplitude and frequency. Damping introduced by the ball bearings supporting the rotor axle was determined using a rheometer by measuring torque over a range of angular velocities in clockwise and counterclockwise direction. These measurements were averaged to obtain the damping characteristics of the system. Only mechanical damping is present in the system. In the scope of this research, mechanical and electrical damping are both approximately linear and can be added up to a total viscous damping term [15]. For this reason, the current test set-up, where total damping is only comprised of mechanical damping ($c = c_m$), is expected to show similar dynamics to a system where total damping is comprised of mechanical and electrical damping ($c = c_m + c_e$). To be able to estimate average power from the physical test a simulated electrical damping coefficient (c_e) was derived from the ratio between total (c_{seiko}) and electrical ($c_{e.seiko}$) damping of the Seiko Kinetic watch, resulting in:

$$c_e = c \cdot \frac{c_{e.seiko}}{c_{seiko}}. \tag{23}$$

The eventual parameters of the physical test set-up can be found in Tab. V.

Parameter	**Value**	**Unit**
Rotor mass, m	$3.20 \cdot 10^{-3}$	kg
Eccentric rotor length, l	$1.64 \cdot 10^{-2}$	m
Viscous damping, c	$3.96 \cdot 10^{-7}$	Nms/rad
Assumed electrical damping, c_e	$2.99 \cdot 10^{-7}$	Nms/rad
Coulomb damping torque, b	$1.60 \cdot 10^{-5}$	Nm
Rotor mass moment of inertia, I_g	$1.33 \cdot 10^{-6}$	kgm^2
Arm length, L	$5.70 \cdot 10^{-1}$	m
Simulation length, T	30.0	s

TABLE V: Parameters of the test set-up.

Arm swing frequency [Hz]	Daily average power, unsprung rotor [μW]	Daily average power, sprung rotor [μW]
0.90	0.34	11.9
1.00	0.99	24.5
1.10	2.09	42.1

TABLE VI: Daily average power of the Seiko Kinetic watch under walking conditions at $\alpha = 1$

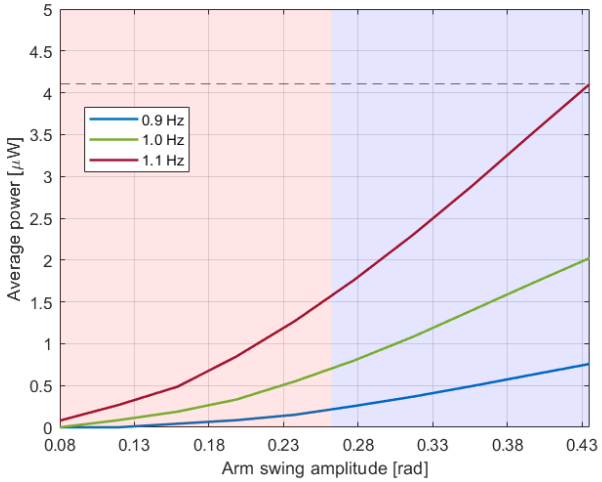

Fig. 7: Simulated average power of the unsprung Seiko Kinetic watch per arm swing amplitude at different arm swing frequencies. The area in red denotes arm swing while walking slow, the area in blue denotes arm swing while walking fast. The maximum simulated average power is marked with dashed black line.

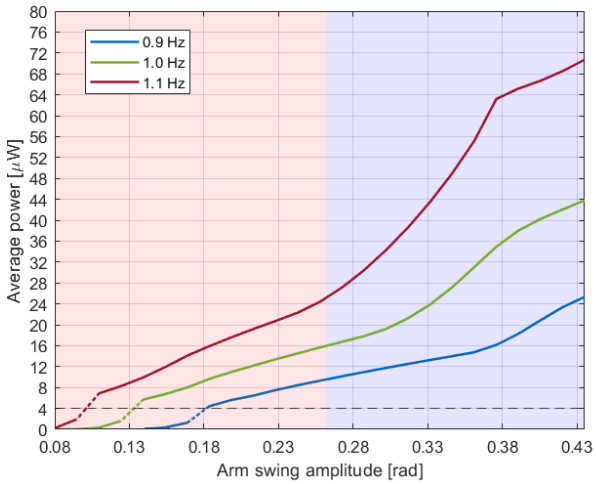

Fig. 8: Simulated average power of the sprung Seiko Kinetic watch per arm swing amplitude at different arm swing frequencies, for $\alpha = 1$. The area in red denotes arm swing while walking slow, the area in blue denotes arm swing while walking fast. The maximum simulated average power of the unsprung Seiko Kinetic is marked with a dashed black line.

IV. Results

The following section discusses the simulation results of the Seiko Kinetic watch (IV-A), the analysis and measurements of the proposed flexure mechanism (IV-A) and the measurements and simulation of the physical test (IV-C).

A. Simulations of the Seiko Kinetic watch

A simulation of average power (Eq. 24) per arm swing amplitude at different frequencies of the unsprung Seiko Kinetic watch was performed, the results of which can be found in Fig. 7. The area in red denotes arm swing amplitudes corresponding to slow walking and the area in blue denotes arm swing amplitudes corresponding to fast walking. The maximum simulated average power is denoted with a dashed black line.

When choosing $\alpha = 1$ and plugging design parameters of the Seiko Kinetic watch into Eq. (14), a stiffness of $k = 1.827 \cdot 10^{-4}$ Nm/rad was found for a sprung variant of the Seiko Kinetic watch harvester. A simulation of the average

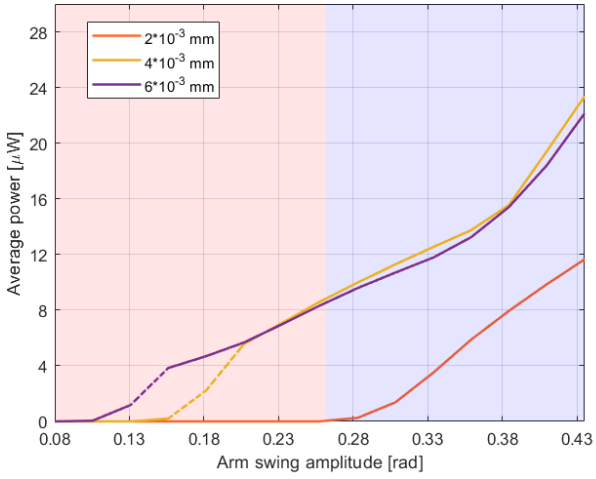

Fig. 9: Average power per excitation input for various eccentric rotor lengths of the sprung Seiko Kinetic, with constant mass m, $\alpha = 1$ and an arm swing frequency of 0.9 Hz. The area in red denotes arm swing while walking slow, the area in blue denotes arm swing while walking fast.

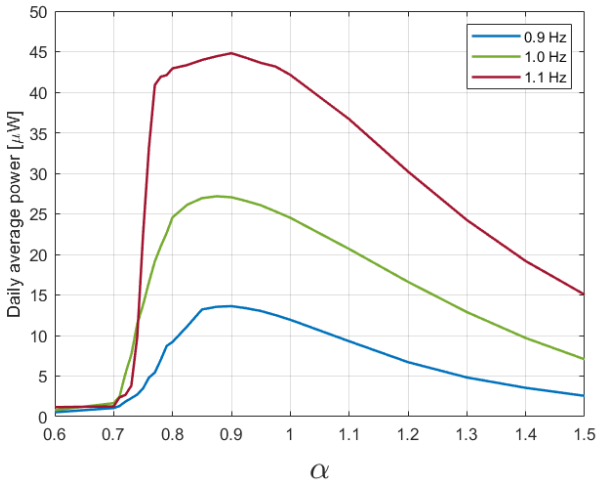

Fig. 10: Simulated daily average power of the sprung Seiko Kinetic watch per value of α for different arm swing frequencies.

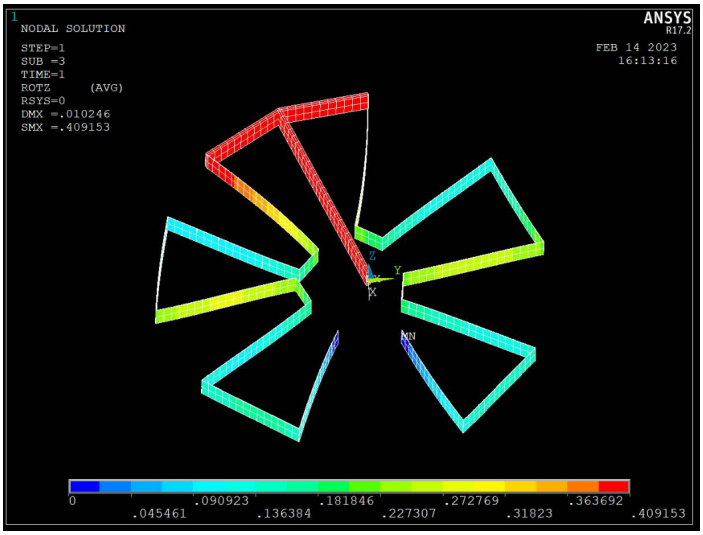

Fig. 11: FEM analysis of the deflection of the flexure mechanism at a torque of 200 μNm.

power per arm swing amplitude at different frequencies of the sprung Seiko Kinetic watch harvester is shown in Fig. 8. The dashed line found in Fig. 7 is shown again for comparison.

Daily average power (P_{da}) per arm swing frequency was determined for walking in both the unsprung and sprung Seiko Kinetic watch energy harvester and shown in Tab. VI. The order of magnitude of the simulated average power of the unsprung mechanism was found to be in accordance with actual measurements performed by Xue et al. [15]. Furthermore, a significant increase in daily average power was observed in the sprung mechanism with respect to the unsprung mechanism. Simulations of average power of the sprung Seiko Kinetic watch were performed with varying eccentric rotor lengths: $2 \cdot 10^{-3}$, $4 \cdot 10^{-3}$ and $6 \cdot 10^{-3}$ m respectively. Mass m and ratio α were kept constant which results in corresponding spring stiffnesses: $9.14 \cdot 10^{-5}$, $1.83 \cdot 10^{-4}$ and $2.74 \cdot 10^{-4}$ Nm/rad respectively. The results can be found in Fig. 9. With a short eccentric length the rotor seems unable to initiate a flipping behaviour at lower amplitudes while for larger eccentric lengths the simulation results converge. Simulations of daily average power of the sprung Seiko Kinetic watch were performed for 26 different values of α at three arm swing frequencies, results can be found in Fig. 10. Maximum average power is achieved at around $\alpha = 0.9$ for each excitation frequency. At lower values of α a sharp decline in simulated daily average power is observed while for higher values of α the simulated daily average power shows a more gradual decline.

B. Flexure mechanism

Mass and eccentric length of the rotor used in the physical test are different than the mass and eccentric length of the rotor found in the Seiko Kinetic watch. Therefore a different stiffness should be implemented to achieve similar dynamics. An appropriate stiffness was derived from the design parameters of the physical test found in Tab. V. When choosing $\alpha = 1$ a corresponding stiffness of $5.15 \cdot 10^{-4}$ Nm/rad was found. A FEM analysis was performed to validate the design. Angular deflection of the rotor was simulated at various torques and is denoted with blue circles in Fig. 12. The visualisation of the simulated deflection at a torque of 200 μNm is shown in Fig. 11. Yield stress of the material was not exceeded according to the FEM analysis. From torque measurements at increasing angular deflection the stiffness

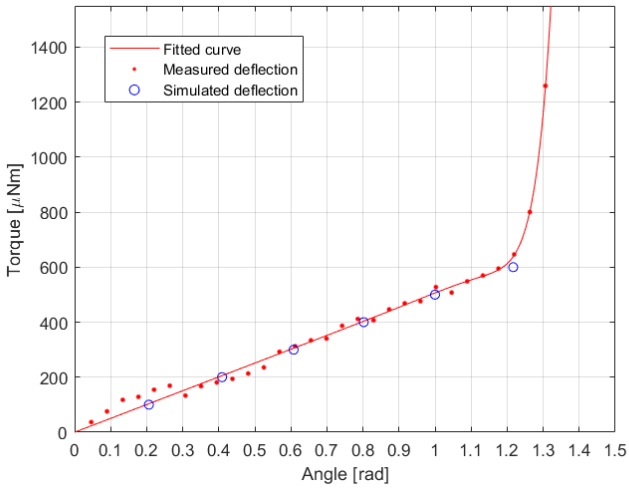

Fig. 12: Measured and simulated torque against deflection of the flexure mechanism.

of the manufactured flexure mechanism was found to be approximately $5.1 \cdot 10^{-5}$ Nm/rad with a steep increase in stiffness due to a physical stop at around 1.2 rad, as can be seen in Fig. 12. Fig. 12 shows the accordance between simulated and measured stiffness of the flexure mechanism up to the location of the measured physical stop. To analyse the effect of a physical stop, three simulations were performed with physical stops at 0.5, 1.2 and 1.6 rad of rotation in both directions. The resulting average power over a swept range of arm swing amplitudes is shown in Fig. 13 and compared to the mechanism without a physical stop and without added stiffness. Increasing the range of the rotor causes the simulation results to converge to the simulation without a physical stop. However, at higher arms wing amplitudes the simulation results become erratic.

C. Physical test

The following section discusses the measurement results of the physical test shown in section III-I. Damping of the system was found to be $3.96 \cdot 10^{-7}$ Nms/rad, determined from the slope of the fitted line through the averaged torque per velocity measurements, as can be seen in Fig. 14. The Coulomb damping torque was found to be around $1.6 \cdot 10^{-5}$ Nm, determined from the first torque measurement. A plot of measurements of the physical test together with simulated average power can be found in Fig. 15. From Eq. 23 electrical damping was assumed to be $3.96 \cdot 10^{-7} \cdot (4 \cdot 10^{-7} / 5.3 \cdot 10^{-7})$ = $2.99 \cdot 10^{-7}$ Nms/rad. Note that total viscous damping of the physical model is in the same order of magnitude as that of the Seiko Kinetic watch which Xue et al. [15] reports

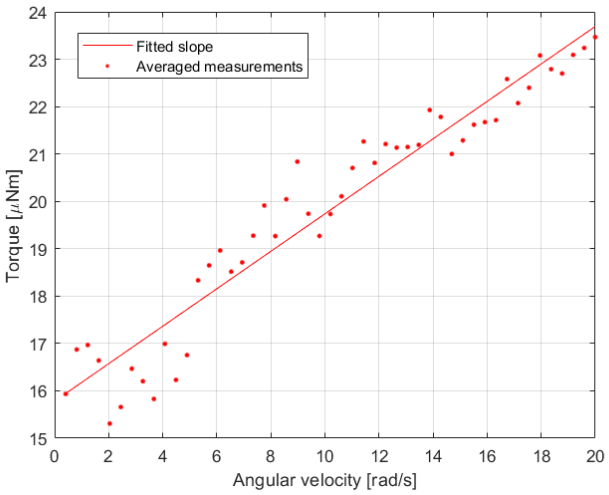

Fig. 14: Measured torque against angular velocity of the physical set-up.

to be $5.3 \cdot 10^{-7}$ Nms/rad. A significant increase in average power is observed for the sprung mechanism with regards to the unsprung mechanism in both the physical test and the simulation. As can be seen in Fig. 15, the simulation shows accordance with the physical test for the sprung harvester. For the unsprung harvester a similar behaviour is observed but with deviation in steepness.

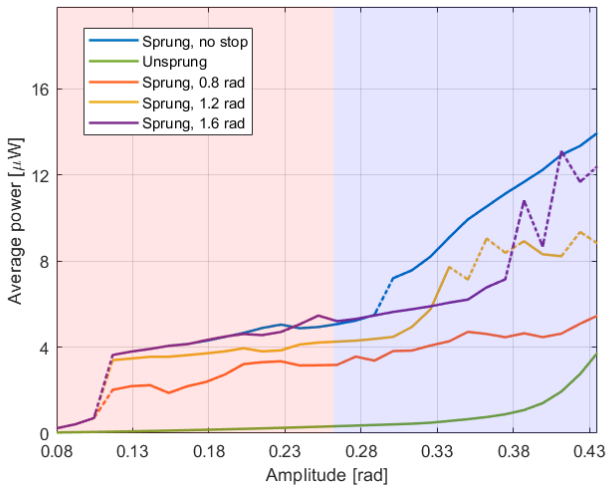

Fig. 13: Simulated average power of the flexure mechanism per arm swing amplitude at 0.9 Hz arm swing frequency, with physical stops at varying locations. The area in red denotes arm swing while walking slow, the area in blue denotes arm swing while walking fast.

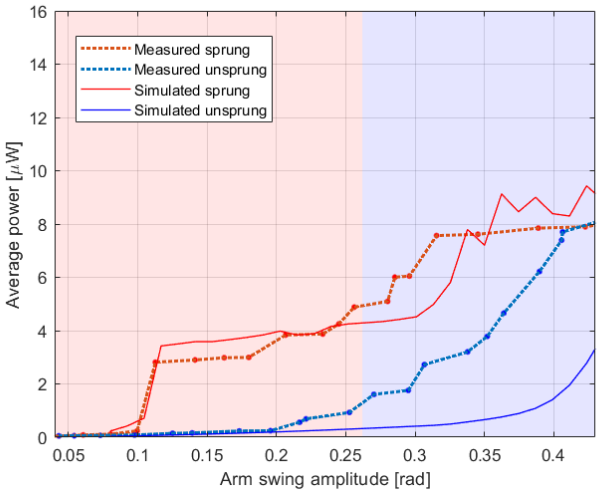

Fig. 15: Measured and simulated average power per arm swing amplitude of the physical test at 0.9 Hz arm swing frequency. For both the sprung and unsprung harvester. The area in red denotes arm swing while walking slow, the area in blue denotes arm swing while walking fast.

V. Discussion

A. Simulation findings

The relation between excitation input and a flipping behaviour of the rotor can be observed in the simulations presented in Fig. 8 and the measurements of the physical test shown in Fig. 15. The moment the system starts exhibiting this flipping behaviour corresponds to the location in the plot where the first jump in average power is observed. For higher arm swing frequencies a lower arm swing amplitude is needed to induce this behaviour as a result of the fact that excitation energy is a function of excitation frequency and amplitude. Based on the analytical formulation of the energy required to flip (E_f), given in section III-D, E_f remains constant over the entire range of operation. However, in the case of a wrist worn harvester under pseudo walking excitation, the frame of the rotor system rotates during arm swing. This causes the required energy to flip the rotor to decrease, benefiting the output power during walking. While considered marginal at small arm swing amplitudes, this effect is considered to have a substantial influence on the power output at large arm swing amplitudes. In the performed simulations and physical tests this behaviour is incorporated.

For the specific case of the sprung Seiko Kinetic harvester, internal friction prohibits the initiation of a flipping behaviour at the lowest excitation input during walking ($0.9\ Hz$ arm swing frequency with an arm swing amplitude of $0.08\ rad$). In this case, a choice of $\alpha = 1$ induces a flipping behaviour the soonest when input energy is increased from an initial lowest value. However, this does not necessarily result in the highest power harvested over the entire range of excitation inputs (P_{da}) as can be seen in Fig. 10. The maximum achievable P_{da} for the Seiko Kinetic harvester under pseudo-walking excitation is found to be around $\alpha = 0.9$ for all arm swing frequencies, as a result of the increase in operational range of the rotor with respect to $\alpha = 1$. However, at even lower values of α a sharp decline in P_{da} is observed. This is due to the shift of the initiation of the flipping behaviour to a higher input energy. For higher values of α a gradual decline in efficiency is observed. This is due to the gradual decrease in operational amplitude of the rotor due to a higher stiffness of the spring. An optimization problem presents itself between moment of initiation of the flipping behaviour and operational range of the rotor. For every use case this optimization results in a particular value for α, based on available energy (amplitude and frequency), and design specifications (e.g rotor weight and eccentric length). Simulation of the system gives insight into an optimal value for α, corresponding to an optimal spring stiffness for that particular system and excitation. It should be noted that the simulation is easily modified for different input excitations and design parameters, the optimization of the Seiko Kinetic harvester subject to walking excitation is merely an example that was chosen to obtain results for an actual harvester.

The approach of optimizing over the full range of presented excitation inputs differs from the optimization approach taken by Halim et al. [13] where the maximum instant average power output of the system is determined, resulting in an optimal spring stiffness for one particular excitation input (arm swing amplitude and frequency). At this input, the stiffness induces resonance of the system, resulting in a significant increase in average power output. However, at other excitation inputs this stiffness does not induce resonance and an increase in efficiency is limited. It is found that this effect is enhanced by the relatively small eccentric length of the rotor proposed by Halim et al., as can be seen in Fig. 9. The eccentric length of the rotor is found to have a large influence on the susceptibility of the rotor to move under an excitation input because mass moment of inertia about the rotational axis is dependent on the eccentric length squared, as is seen in Eq. (15). At low excitation inputs a small eccentric length could result in a system that is not able to overcome torque due to damping and friction. On the other hand, a small eccentric length results in a low optimal stiffness (around $\alpha = 1$). Therefore, the system is able to undergo large amplitude motion at resonance, increasing power output and resulting in the peak efficiency observed by Halim et al.. However, this resonance occurs at a high excitation input, limiting the system's ability to efficiently harvested energy at a broad bandwidth of (low energy) excitation inputs.

The system presented in this work is not designed for resonance, but rather the optimized moment of initiation of the discussed flipping behaviour of the rotor. Rather than a peak in average power this creates a plateau in average power which gradually increases over the range of presented excitation inputs. Although the peak average power at resonance is higher than the mean average power found in the current research, the overall power is increased. From this insight it can be concluded that the best approach for optimization of stiffness is dependent on the system's excitation input. For systems of which the excitation input is dominated by one excitation, a harvester designed for resonance with small eccentric length might be optimal, resulting in a low optimal stiffness and large operational amplitude. For a system that is subjected to a range of excitation inputs, the optimal stiffness depends on the optimal moment of induced flipping behaviour of the rotor, with corresponding α. When the harvester is subjected to a range of excitation inputs, the eccentric length of the harvester should be large enough to allow for enough inertia at the lowest excitation input to overcome resistive forces due to friction and damping (Fig. 9). It is found that in current existing rotational energy harvesters the eccentric length should be maximised within the design space for optimal daily average power.

B. Flexure mechanism

Stiffness measurements show good accordance with the stiffness determined by FEM analysis up to the point where the predicted physical stop is met. The exact location of this point is derived from the rheometer measurements to feed back into the simulation. The effect of a physical stop is investigated by performing simulations of the test set-up with constant stiffness but varying physical stop locations (Fig. 13). It is

found that a physical stop limits the harvested average power at higher input energy with regards to a harvester without a physical stop. However, the simulated average power is still significantly higher for sprung harvesters with a physical stop than for an unsprung harvester. A larger operational range results in a higher power benefit, which yields the conclusion that operational range should be maximised. A finite range of motion induces a 'hammering behaviour' of the rotor, this is observed at the point where input energy is high and the rotor encounters one of the physical stops with a high velocity. This causes the rotor to bounce back and, at an input energy that is high enough, flip to the other side again. Due to the chaotic nature of this behaviour the simulation results become erratic (i.e. visible in the higher amplitude simulations).

C. Physical test

The main purpose of the physical test is the proof of concept of the flexure mechanism to create a sprung rotational harvester. Furthermore the physical test is used to understand the relation between the simulation and the physical world. Measurement results found in Fig. 15 show the increase in possible harvested power between the sprung and the unsprung rotor under a pseudo walking input. Because no power is actually generated it is not yet possible to define the exact benefit of this sprung rotational energy harvester, however a strong argument is made for the benefit of the sprung mechanism under these excitations because the denoted 'average power' in Fig 15 is calculated using velocity data from the test and a realistic electrical damping coefficient.

The pseudo-walking excitation which is used as input for the current research is a simplification of actual human movement. While planar movement of a stretched arm is the dominating form in walking, out-of-plane motion and bending of the elbow are usually present. Further research could include the fabrication of a prototype implementing the proposed flexure mechanism and testing this for actual wrist movement. The difference between measured and simulated data is thought to be from imperfections in the test set-up. An imperfect sine input from the stepper motor is regarded to be the the main cause of the dissimilarities between measured and simulated data. Fig. 16 shows both the input used in simulation and in the physical test for the test with an arm swing amplitude of 12 degrees. It is found that especially the unsprung mechanism is sensitive to these deviations. The increase in angular velocity of the arm, visible in Fig. 16 between each peak and trough is thought to be the cause of the steeper increase in average power for the unsprung physical test compared to the simulation. When measured arm swing is directly used as input for the simulation an unreasonably high sensitivity to small deviations is found. It is thought that this is due to the infinitely stiff simulated coupling between shoulder joint and wrist, whereas the arm in the physical test is thought to introduce some damping term. Further development of the simulation could be focused on incorporating a realistic damping term or simulating the deformations in the arm. However, the latter would significantly increase simulation time.

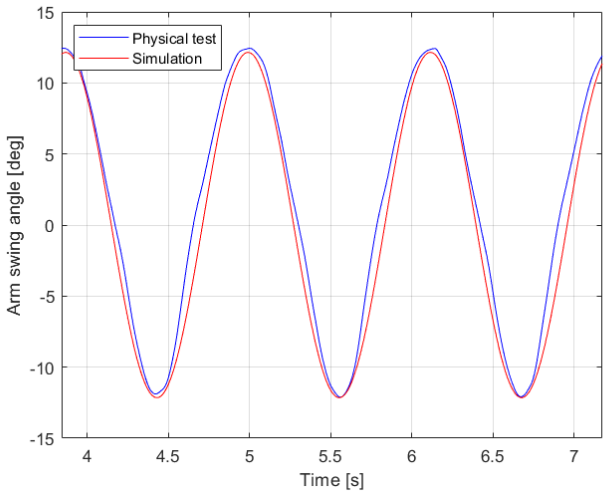

Fig. 16: Pseudo arm swing of the physical test compared to arm swing in the simulation

VI. Conclusion

In this paper a generalised model for sprung rotational energy harvesters is presented from which a relation is derived between torsional stiffness and rotor design parameters. An understanding is attained of the behaviour of a sprung rotational harvester subjected to a range of excitation inputs rather than one. The focus is placed on energy harvesting for wearables undergoing a pseudo-walking excitation for which both a simulation and a physical test are performed, these show a significant improvement in daily average power (P_{da}) for a sprung rotational harvester in relation to an unsprung rotational harvester. It is observed that this increase in power is due to the rotor flipping from side to side under the imposed excitation. A compliant design is proposed for the implementation of a rotational stiffness in existing rotational energy harvesters without requiring major design changes. This is achieved by introducing flexures in the plane of the rotor. A physical test serves as a prove of concept for the proposed flexure mechanism, which is manufactured and tested on a larger scale. The simulation and physical test show good accordance for the sprung mechanism, for the unsprung mechanism some divergence is observed. The implementation of the compliant flexure mechanism to add stiffness to existing automatic winding systems is found to significantly benefit energy harvesting in wearables.

Acknowledgment

The research for this paper was commissioned by Flexous and Kinergizer. Flexous specializes in the design of compliant solutions for the challenges in the watchmaking industry. I would like to thank everyone from Flexous and Kinergizer for providing a comfortable, productive and enjoyable work environment. Furthermore, I would like to thank Werner van de Sande, Joep Meij and Gerard Dunning for their supervision

and guidance and Alden Yellowhorse for his assistance with performing the finite element analysis which was set-up by him on behalf of Flexous.

REFERENCES

[1] S. Priya and D. Inman. *Energy Harvesting Technologies*. Springer, New York, 2009.

[2] P. D. Mitcheson, E. M. Yeatman, G. Kondala Rao, A. S. Holmes, and T. C. Green. Energy harvesting from human and machine motion for wireless electronic devices. *Proceedings of the IEEE*, 96:1457–1486, 2008.

[3] N. M. Turab, H. A. Owida, J. I. Al-Nabulsi, and M. Abu-Alhaija. Recent techniques for harvesting energy from the human body. *Computer Systems Science and Engineering*, 40:167–177, 2022.

[4] B. Pozo, J. Ignacio Garate, J. Ángel Araujo, and S. Ferreiro. Energy harvesting technologies and equivalent electronic structural models - review. *Electronics (Switzerland)*, 8, 5 2019.

[5] J.A. Paradiso and T. Starner. Energy scavenging for mobile and wireless electronics. *IEEE Pervasive Computing*, 4(1):18–27, 2005.

[6] S. Khalid, I. Raouf, A. Khan, N. Kim, and H. Soo Kim. A review of human-powered energy harvesting for smart electronics: Recent progress and challenges. *International Journal of Precision Engineering and Manufacturing - Green Technology*, 6:821–851, 8 2019.

[7] K. Fan, M. Cai, H. Liu, and Y. Zhang. Capturing energy from ultra-low frequency vibrations and human motion through a monostable electromagnetic energy harvester. *Energy*, 169:356–368, 2 2019.

[8] M. A. Halim, T. Xue, R. Rantz, Q. Zhang, L. Gu, K. Yang, and S. Roundy. Fabrication and characterization of a wrist-driven rotational energy harvester using multiple plucked piezoelectric unimorphs. *Journal of Physics: Conference Series*, 1407, 12 2019.

[9] P. Pillatsch, E. M. Yeatman, and A. S. Holmes. A piezoelectric frequency up-converting energy harvester with rotating proof mass for human body applications. *Sensors and Actuators, A: Physical*, 206:178–185, 2 2014.

[10] E. M. Yeatman. Energy harvesting from motion using rotating and gyroscopic proof masses. *Proceedings of the Institution of Mechanical Engineers, Part C: Journal of Mechanical Engineering Science*, 222:27–36, 1 2008.

[11] H. Fu, X. Mei, D. Yurchenko, S. Zhou, S. Theodossiades, K. Nakano, and E. M. Yeatman. Rotational energy harvesting for self-powered sensing. *Joule*, 5:1074–1118, 5 2021.

[12] S. Roundy, R. Rantz, T. Xue, and M. Abdul Halim. Inertial energy harvesting for wearables system architectures, power generation limits and transducers. 2018.

[13] M. A. Halim, R. Rantz, Q. Zhang, L. Gu, K. Yang, and S. Roundy. An electromagnetic rotational energy harvester using sprung eccentric rotor, driven by pseudo-walking motion. *Applied Energy*, 217:66–74, 5 2018.

[14] M. P. Ford, R. C. Wagenaar, and K. M. Newell. Arm constraint and walking in healthy adults. *Gait and Posture*, 26:135–141, 6 2007.

[15] T. Xue, S. Kakkar, Q. Lin, and S. Roundy. Characterization of micro-generators embedded in commercial-off-the-shelf watches for wearable energy harvesting. *SPIE Smart Structures and Materials*, 9801:98010O, 4 2016.

[16] D. Machekposhti, N. Tolou, and J. L. Herder. A review on compliant joints and rigid-body constant velocity universal joints toward the design of compliant homokinetic couplings. *Journal of Mechanical Design, Transactions of the ASME*, 137, 2015.

[17] J. Yu, P. Xu, S. Minglei, Z. Shanshan, B. Shushing, and Z. Guanghua. A new large-stroke compliant joint micro/nano positioner design based on compliant building blocks. *ASME/IFToMM International Conference on Reconfigurable Mechanisms and Robots*, page 409–416, 01 2009.

[18] L. L. Howell. Compliant mechanisms. *21st Century Kinematics*, pages 189–216, 2013.

[19] R. Rantz, M. A. Halim, T. Xue, Q. Zhang, L. Gu, K. Yang, and S. Roundy. Architectures for wrist-worn energy harvesting. *Smart Materials and Structures*, 27, 3 2018.

[20] D. Rixen. Engineering dynamics. Lecture Notes. Delft University of Technology, 9 2008.

[21] H. Goldstein. *Classical Mechanics*. Addison-Wesley, 1980.

[22] T. Xue, S. Williams, R. Rantz, M. Abdul Halim, and S. Roundy. System modeling, characterization, and design considerations for generators in commercial watches with application to energy harvesting for wearables. *IEEE/ASME Transactions on Mechatronics*, 23:2515–2524, 10 2018.

[23] J. Herder. *Energy-free systems: Theory, conception, and design of statically balanced spring mechanisms*. PhD thesis, Delft University of Technology, 2001.

[24] F. Danion, E. Varraine, M. Bonnard, and J. Pailhous. Stride variability in human gait: The effect of stride frequency and stride length. *Gait and Posture*, 18:69–77, 2003.

[25] M. Staffan Johansson, M. Korshøj, P. Schnohr, J. Louis Marott, E. Irene Bossano Prescott, K. Søgaard, and A. Holtermann. Time spent cycling, walking, running, standing and sedentary: A cross-sectional analysis of accelerometer-data from 1670 adults in the copenhagen city heart study. *BMC Public Health*, 19, 10 2019.

Appendix A
Literature Review

The Implementation of Compliant Joints in Rotational Energy Harvesters for Wearables

Sam van den Oever

***Abstract*—The interest to power small scale wearable electronics by harvesting kinetic energy from their wearer is increasing. The most prominent harvester designs are found to be rotational energy harvesters using either electromagnetic, electrostatic or piezoelectric transduction to convert movement into electricity. These systems can be made more efficient by implementing compliant joints, negating friction from bearings. A classification of state-of-the-art compliant joints is made and their compatibility with the different transducers is discussed. The stiffness that is introduced by implementing compliant joints is found to possibly benefit the harvester's power output significantly due to resonance at specific human input excitation. The stiffness of current compliant joints should however be lowered significantly for resonance to occur, which is regarded as an interesting topic for further research.**

***Keywords*—Energy Harvesting, Compliant Mechanisms, Transducers, Wearables,**

I. Introduction

Recently the interest in sustainable solutions for energy supply has risen explosively. In the field of small scale electronics this trend has also caught up. Aside from improving batteries to store power, the possibility for energy harvesting within a device is gaining a lot of attention [1]. This holds for a variety of devices including wireless sensors, medical devices and micro-robotics [2]. Another field in which energy harvesting already has a longer history is horology. Automatic winding within wristwatches has made a long process of improvements and current-day mechanical wristwatches have a sophisticated auto winding system allowing these devices to stay operational when worn [3].

Nowadays however, most wearable devices are electronic and require batteries to function. Instead of a mainspring being wound, these devices need a way to charge their battery from ambient energy sources. To be able to self-power a wearable electronic device a micro-generator should be designed which converts ambient energy into electricity. Wearable devices are subjected to a number of different ambient energy sources (Kinetic, Thermal, Cardiovascular, etc.) and literature shows a large variety of harvesting and transduction types [4]. One of the most prominent sources of ambient energy investigated is kinetic energy produced by the body. For motion energy harvesters there exist a few types of transduction which can be categorised into: electromagnetic (inductive), electrostatic (capacitive) and piezoelectric transducers [5]. Each method has it's own advantages and disadvantages, and different situations require different transduction methods.

Human motion is characterised by ultra-low frequency excitations and large amplitudes. From literature it is seen that this type of energy is often harvested using a rotating proof mass guided with a bearing which is exited during daily activities, transforming random input motion into a rotational generator input [2].

The electrical energy harvested from human movement is very minimal, often enough to power a wearable under specific input conditions but still in need of improvement for widespread implementation. A way to increase efficiency is by eliminating friction from the bearings by making the system compliant.

Compliant mechanisms gain their functionality from the bending of elastic members in a specifically designed topology. Unlike conventional mechanisms, compliant mechanisms can be made from one part while achieving complex motion, granting them some key advantages over traditional mechanisms [6]: Friction is negated because of the direct transmission of movement, wear is reduced with the reduction of connecting surfaces, the system is highly scalable and no lubrication is required. However, compliant mechanisms also have specifications which bound the design to certain functionality, range of operation and introduced stiffness create a characteristic motion behaviour which creates a fundamentally different system. In this article the bridge is made between the required motion input for different transducer types and the motion that can be facilitated by compliant rotational joints.

Transduction methods found in literature are categorised and their compatibility with compliant rotational mechanisms is evaluated. This is done by defining range of motion and rotational stiffness as criteria and using these values to compare feasible joint output and required transducer input. By combining the two, a resonant system is created. This is further researched in the paper and a possible benefit is found. To be able to utilise this benefit an approach for future research is suggested.

II. Method

A. Scope

This literature review is focused on rotational energy harvesting for electronic wearable devices. Within this scope the most prominent limitations are: size, generated power and input excitation [2]. Logically the energy harvesting system inside a wearable can not exceed dimensions that would cause inconveniences to the wearer. Representative dimensions are deducted from existing wearable devices, in particular wrist-worn wearables.

The minimum power that is to be generated by an energy harvester during regular everyday use is defined from the power usage of typical electronic wearables. It's rather difficult to strictly follow this criterion because generated power is

strongly dependent on the generator and the motion input from the mechanism of an energy harvester, which are both often still novel prototypes proposed in literature and not tested extensive enough.
Furthermore, the scope is bound by the input frequency from ambient motion, where human movement is considered to be the energy source. The input excitations are considered to be ultra-low frequency (around 1 Hz) with relatively high amplitudes (multiple times larger than the device's dimensions), and are also typically irregular of nature [7], [8], [9].
Rotational energy harvesters (REH's) are considered because rotational systems have the advantage to harvest energy from both rotational and linear input excitations [10]. A linear input energy harvester is only able to generate energy under linear excitation along the axis of the proof mass mechanism. All energy from movement that is not on this axis is lost. Pure rotation around the centre axis is also left unharnessed. A rotating proof mass on the other hand is able to harness energy from linear movement in multiple axis and rotation around the centre creates a relative movement of the proof mass with respect to the wearables' housing. Furthermore, under the right excitation, a rotating proof mass can be swung and left to move freely whereas a linear energy harvester is constrained by a physical stop imposed by the design dimensions [10]. REH's are therefore more suitable for human movement, which is multi-directional and irregular. Whereas a linear energy harvester might be more suitable to be implemented in mechanical systems with uniaxial, small amplitude and regular movements.
In this article the possibility to facilitate the rotational input for REH's using compliant joints is reviewed. These rotational compliant mechanisms are discussed and bundled by Farhadi et. al. [11]. Further research on compliant rotational mechanisms is done, but it is found that the review done by Farhadi et. al. still gives a representative overview of the possibilities of state-of-the-art compliant joints.

B. Search Method

For this literature research the databases Scopus, Science direct and Google Scholar were consulted. Furthermore information was gathered by consulting experts at the company where this research is performed, Flexous.

C. Categorisation

In this article it is attempted to bridge the gap in literature between rotational small-scale energy harvesters and compliant joints. To be able to compare these two fields a categorisation has to be made after which compatibility is reviewed. These categorisations are made by comparing existing literature and combining literature with large common ground to create well substantiated categories.

1) Transduction Mechanisms: Within the scope of electronic wearables there exist three main types of electrical generators: Electromagnetic, Piezoelectric and Electrostatic (Triboelectric). An extensive literature survey on these three methods is performed by Khalid et. al. [12]. Within the current article these transduction methods are reviewed under rotational input. There exists a considerable amount of literature on REH's, which is bundled and reviewed by Fu et. al. [2].

Electromagnetic
Electromagnetic transduction is based on the relative movement of a magnet to a coil [13]. At large scale, electromagnetic transduction is by far the most implemented technique for power conduction, from the dynamo on a bike to the generator in a wind turbine. At smaller scale, in the scope of this article, electromagnetic transducers are also represented in literature. However on this scale, at lower frequencies, electromagnetic generators quickly decline in efficiency, with maximum power scaling to characteristic length and frequency as shown in Eq. 1 [14].

$$P_{max} \propto L^5 \omega^2 \tag{1}$$

The voltage produced by a magnet moving over a coil is denoted by Eq. 2

$$V = -N \frac{d\phi}{dx} \frac{dx}{dt} \tag{2}$$

Where N denotes the number of coil windings, $\frac{d\phi}{dx}$ denotes the magnetic flux change, which is dependent on design parameters like the strength of the magnet used and the diameter of the coil wires, and $\frac{dx}{dt}$ denotes the velocity which is related to the frequency and amplitude of the system under non-continuous motion. When all other parameters remain constant the voltage drops at low frequencies.

Rotational electromagnetic generators found in literature often comprise of an eccentric proof mass (rotor) rotating over a static surface (stator). With either permanent magnets attached to the rotor and coils to the stator, or the other way around, creating a so called 'axial-flux generator' [14], of which multiple are found in literature [15],[16], [17] and of which the workings of the latter are shown in Fig. 1. This type of generator is non-resonant and relies on a proof mass being swung around during movement of the wrist. Electricity is produced when the magnet moves over the wires in the coil inducing a change in flux when it passes the next winding. This change in flux creates a current which can be used to generate power. For this system to work as efficient as possible the magnet should be introduced to as many new windings as possible, which increases the change in flux. The range of motion required by the magnet to pass a coil is found in literature to range between roughly 45 and 90 degrees. All presented literature states that sufficient energy is produced to power small scale electronic devices. This is derived from tests done with prototypes and by simulations [15], [16], [17].

Electrostatic
The second conventional transduction mechanism is electrostatic conversion. Electrostatic conversion of motion to electricity works on the principle of moving charged electrodes relative to each other [18]. When work is performed against

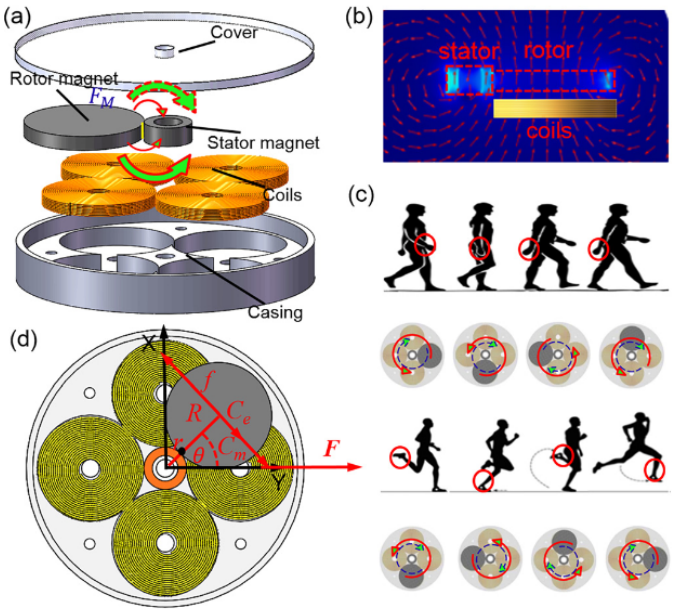

Fig. 1. "(a) The physical structure of the REH; (b) the magnetic field distribution of the stator and rotor; (c) two typical application scenarios for the REH, where the rotor magnet of the REH attached on the wrist and ankledoes clockwise and anticlockwise rotation around the center stator magnet;and (d) physical model of the REH when the rotor magnet rotates.203901-2 Liuetal.Appl. Phys. Lett.113, 203901 (2018)." [17]

the electrostatic force, a current is produced which can be harvested. This work is again performed by the use of a proof mass which is excited during motion of the wearable.
At large scale, electrostatic transduction is not efficient, however at the scale of microelectromechanical systems (MEMS) this transduction method becomes viable [18]. Within the scope of rotational micro-generators there are some examples of a rotational electrostatic micro-generator in literature, they are bundled by Fu et. al. [2]. In principle a separate voltage source is required to effectuate an initial voltage source for an electrostatic generator to work. This can however be negated by implementing an electret in the system which can be seen as the electric equivalent of a permanent magnet [19]. Most rotational electrostatic energy harvesters found in literature implement this system [20], [21], [22]. The schematic design of a rotational electrostatic energy harvester is shown in Fig. 2.

Piezoelectric

Piezoelectric materials generate an electric potential when strain is applied to them. From this, electricity can be harvested. Piezoelectric material is stiff and brittle and energy is most often generated by the (slight) bending of a piezoelectric cantilever beam [23]. The brittleness of a piezoelectric material does not allow for large rotations, so to generate energy from a rotational input these cantilevers have to be excited shortly, after which they can oscillate in their natural frequency. This process is called plucking.

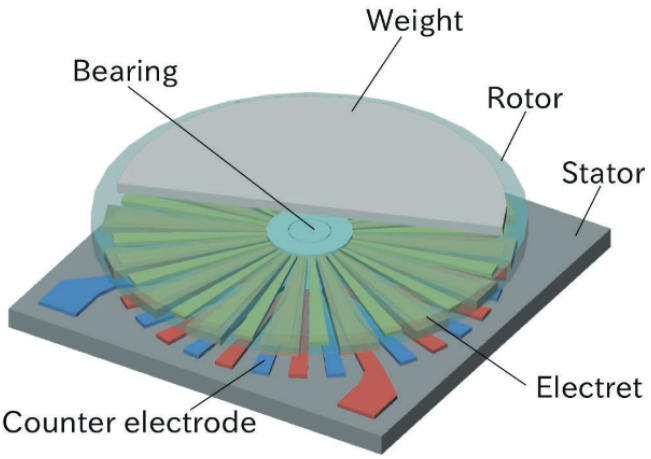

Fig. 2. "Schematic of rotational electret energy harvester" [21]

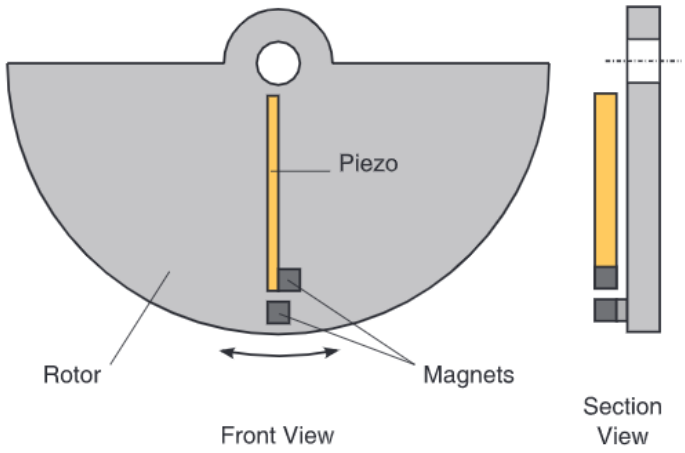

Fig. 3. "Principle of operation of the rotational beam-plucking energy harvester." [24]

Again this principle utilises a rotating proof mass to harvest the low-frequency input excitations from human movement. All piezoelectric REH's found by the author implement the principle of plucking. When plucked, the piezoelectric cantilever will oscillate at it's natural frequency at which it experiences enhanced amplitudes. Because higher amplitudes result in higher material strain, the piezoelectric material is able to produce more energy. This principle is called frequency up-conversion which causes the low-frequency input to be converged to higher frequencies at which the piezoelectric material is more efficient. Frequency up-conversion within energy harvesting is further explained by Wu et. al. [25]. Pillatsch et. al. proposes such a design with a single cantilever being plucked [24], this system is shown in Fig. 3. A mean power in the range of tens of microwatts is achieved during walking which is claimed (but in need of further research) to possibly outperform the energy harvester of the Seiko Kinetic. The Seiko Kinetic, as well as the ETA autoquartz

Type of energy harvesting	Advantages	Disadvantages	Challenges
Piezoelectric	High energy density High voltage output High capacitance Small mechanical damping No separate voltage source	Difficult integration Poor coupling High impedance, low current Need of piezoelectric material Self-discharge at low frequency	Ultralow frequency of human Brittleness and rigidity of Piezo materials Complex human motion Toxicity of piezo materials
Electromagnetic	No seperate voltage source High output current Low output impedance Small mechanical damping No need of contacts Robust and durable	Low efficiency at low frequency Coil losses Difficult integration Low voltage Complicated miniaturization	Designing a flexible system Difficulties of integration Difficulties in miniaturizing
Electrostatic	Low operation frequency Device flexibility High power density High conversion efficiency	Mechanism not fully understood Difficult to integrate Low current at high voltage Durability	Inflexibiliy of electrode Humidity Washability Biocompatibility

TABLE I. ADVANTAGES, DISADVANTAGES AND CHALLENGES OF THE PROPOSED TRANSDUCTION METHODS. [12]

implement an electromagnetic generator and, by the authors knowledge, are the only commercially implemented kinetic energy harvesters for an electronic wearable. When power production of the Seiko Kinetic is matched or outperformed by the piezoelectric harvester this would show feasibility for a rotational piezoelectric energy harvester to power small scale electronic wearables.
An overview of the advantages and disadvantages of the transduction methods discussed earlier is presented by Kahlid et. al. [12] in the form of a table. This table is shown in Tab. I. The table also denotes the challenges that arise when implementing a certain transduction method in a design.

2) Compliant Rotational Joints: Farhadi et. al. performs an extensive review on state of the art compliant rotational joints [11]. Different designs are bundled and categorised and shown in Fig. 4. Furhter literature research on compliant rotational joints is done and additional designs proposed in literature are found, they can be found in section VI of this review. However, no mechanism is found which significantly changes the range in characteristics from all mechanisms bundled by Farhadi et. al. Therefore, these mechanisms are considered to be a good representation of the current state-of-the-art on compliant rotational joints. They are also easy to compare because they are modeled with the same material properties and at approximately the same size, which makes the comparative plot seen in Fig. 5 credible. In this figure the range of motion and the rotational on-axis stiffness of the bundled compliant joints is compared, which visualises the large range in characteristics compliant joints have. Although the paper by Farhadi et al. has the goal to review these designs with regards to kinetic coupling, the categorisation can also be used to review the designs with regards to solely rotational motion input. The assumption is made that a compliant rotational joint could couple the rotational motion of a proof mass as the input motion for a generator. This system replaces the bearing proposed in previous literature on REH's and imposes different characteristics. Farhadi et. al. makes the distinction between notch type mechanisms and leaf spring compliant joints, they

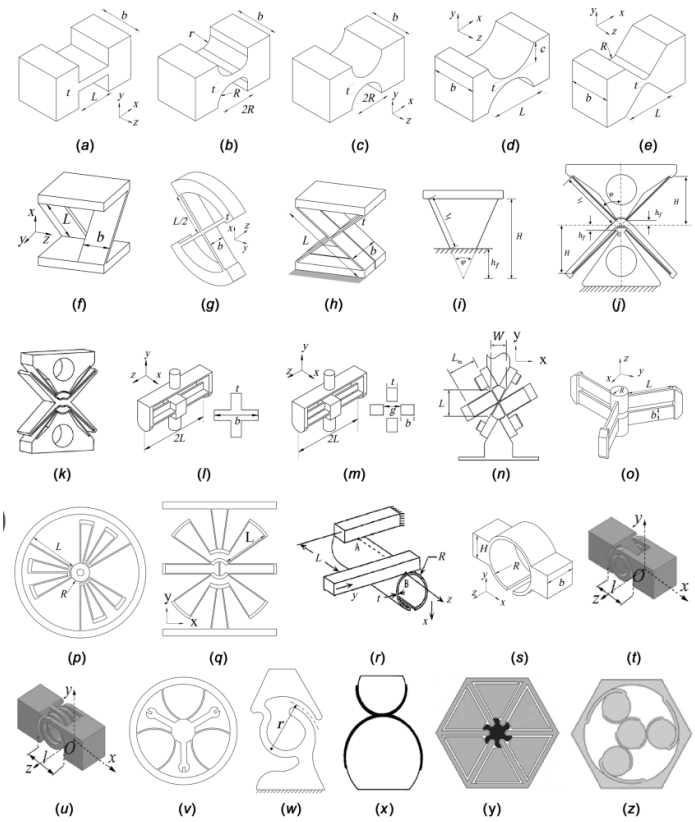

Fig. 4. Collection of state of the art compliant joints. [11]

are modeled with the same material properties and at similar scale. An important distinction in range of motion and stiffness can be made between notch type flexures (4(a,b,c,d,e)) and leaf spring compliant joints (4(f,g,h,i,j,k,l,m,n,o,p,q)), where notch type flexures have relatively high stiffness and a small range of motion and leaf spring compliant joints have significantly lower stiffness and higher range of motion.

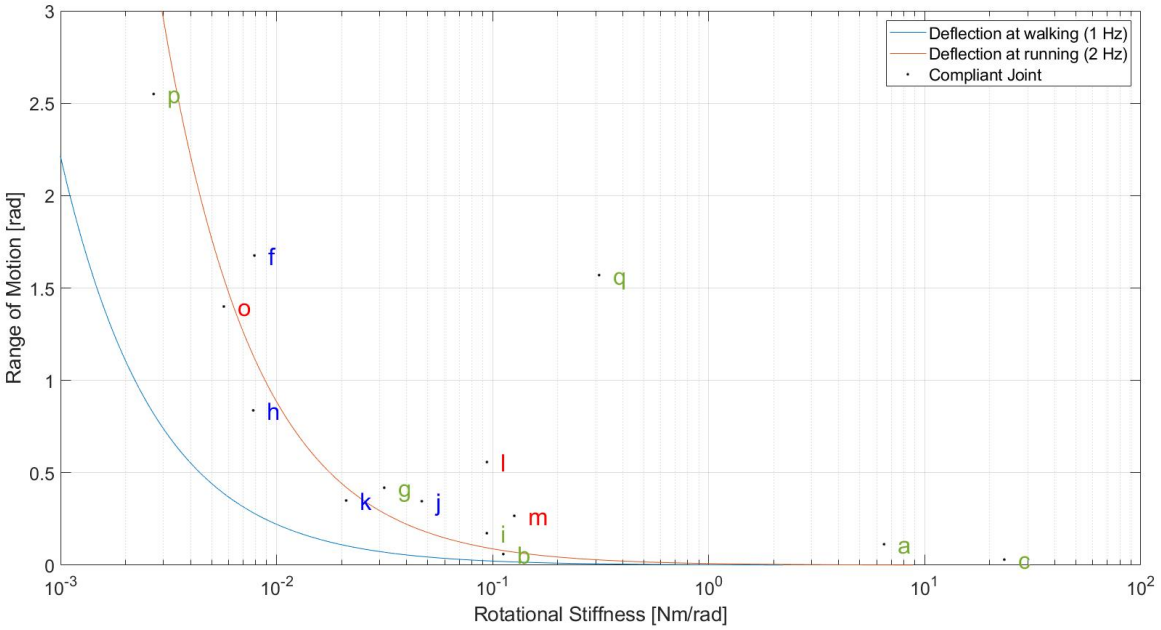

Fig. 5. Scatter plot comparing the mechanisms bundled by Farhadi et. al. [26] and showing the maximum deflection of a rotational harvester corresponding to implemented stiffness

To classify the different compliant joints, three characteristics are defined with which compatibility can be evaluated: *range of motion*, *stiffness* and *size and planarity*. They are explained in the following section and visualised for each joint using a scatter plot, which can be found in Fig. 5. To gain an understanding of what the addition of a stiffness does to the range of motion of an energy harvester, a back-of-the-envelope calculation is done. The minimum and maximum frequencies of human arm-swing (between 1 Hz (walking) and 2 Hz (running) [27]) are used to calculate the approximate deflection caused by an eccentric rotor that is expected when subjected to a certain rotational stiffness. This is deducted from the arm swing amplitude, eccentric mass, arm length and rotor length, taken from the prototype proposed by Halim et. al. [28]. These values are plotted in Fig. 5 and show the range of motion that should be facilitated by a compliant joint to obtain maximum deflection at it's implemented stiffness. The assumed values and calculations can be found in section VI.

Range of Motion

Range of motion is defined by the angle the joint can make about its rotational axis before failure or before a physical stop. This will be viewed as the range of operation the compliant joint can facilitate and consequently the range at which the dedicated transducer can operate.

Stiffness

Compliant joints inherently introduce a stiffness and are therefore sprung systems with a characteristic resonance behaviour. The stiffness of a compliant joint is of great influence on the system's natural frequency, which is important to consider in energy harvesting because a system is able to harvest significantly more energy around it's natural frequency. By implementing a compliant joint like the ones proposed in [11] an energy harvester becomes a resonant system instead of a non-resonant system.

There is an exception for specially designed compliant mechanisms, so called 'near-zero-stiffness' compliant mechanisms. The mechanism proposed by Morsch et. al. is statically balanced by utilising opposing leaf-springs, creating a system that has virtually no stiffness around it's axis of rotation, with a range of approximately 140 degrees [29]. However, it should be noted that this system has large dimensions which make it unsuitable to be scaled down to the scale of energy harvesters. The same holds for the mechanisms proposed by Kuppens et. al. [30], where the 'near-zero-stiffness' behaviour is accomplished by using an additional leaf spring set up, taking up significant space.

Size and planarity

The size and planarity of a mechanism are key characteristics to define if a mechanism is suitable to be implemented into wearables. Although compliant mechanisms are usually very scalable, it is still possible to make a classification on

this characteristic. The aspect ratio of the dimensions of a mechanism could for example show the infeasibility of the implementation of a joint design into a wearable. Furthermore, the design of a watch or wearable is planar [31], utilising slender components to maintain ergonomic dimensions. For a compliant joint to be implemented this criterion should be kept. The size and planarity of the mechanisms is rated using a scoring method based on the feasibility of implementing the mechanism in a small scale wearable. This comes down to the scalability of the system and if the aspect ratio's of the system are not compromised when scaling down to the size of a wearable. In the scatter plot seen in Fig. 5, colours indicate the size rating: green indicates good feasibility to be operational at wearable scale, blue indicates that the design facilitates down-scaling to wearable size but functionality might deteriorate and red indicates that down scaling to the size of a wearable is thought to be infeasible.

D. Criteria

A criterion for a compliant joint to be compatible with a transduction method is sufficient range of motion. To achieve functionality different transduction methods require different ranges of motion. This is elaborated upon for all three transduction mechanisms in the following section.

Range of motion: Electromagnetic

As stated before, rotational electromagnetic transducers rely on the rotation of a magnet over a set of coils. This magnet creates a change in flux inducing a voltage according to Eq. 2. To increase the amount of electricity generated by an electromagnetic generator a few things can be altered: A higher velocity of the magnet, using smaller wire diameters to increase magnetic flux change, increasing the number of windings per coil or increasing the working range of the magnet per excitation, causing the generator to have longer periods of generation time per swing of the proof mass.
Velocity of the magnet is limited by the nature of the input motion, which is low frequency human motion with large amplitude. This is often paired with relatively low velocity.
The diameter size of the wires used in the coils is limited by the maximum electrical resistance. By decreasing this diameter the electrical resistance becomes higher than the load resistance which will eventually prohibit power production.
Furthermore, the number of windings per coil and the amount of coils is limited by the available design space.
This leaves the most obvious way to increase energy production which is increasing the working range of the magnet which results in more flux changes in the coils. The influence of the magnitude of the amplitude can be seen in the calculation for the theoretical maximum power production by a non-resonant rotational harvester which is evaluated in [2], this theoretical maximum is shown in Eq. 3

$$Pmax = \frac{I * \omega^3 * \Omega^2}{4} \tag{3}$$

Where I denotes the mass moment of inertia of the proof mass, ω the excitation frequency and Ω the amplitude.
This increase in power with larger amplitudes can also be seen in experimental results found in [16] and [17]. The generators proposed in literature are tested when attached to different parts of the body. Sufficient energy to power small scale electronic wearables was found under normal walking conditions which is characterised by large amplitude (larger than the device dimensions). Niroomand et. al. states maximum power production at excitations of 180 degrees where the magnetic pole pairs are able to pass three entire coils [16]. Even though it is difficult to determine a minimum range an electromagnetic transducer requires to function, it can be stated that the larger the amplitude the better, for a non-resonant rotational electromagnetic harvester.

Range of motion: Electrostatic

An electrostatic generator produces energy when strips of opposing charge are moved relative to each other. With regards to the motion input, rotational electrostatic generators are similar to electromagnetic generators in the sense that a larger stroke generates more energy [22]. The larger the stroke, the more electrodes the electret passes by. With every passage of an electrode alternating current is created, which determines the eventual energy production.

Range of motion: Piezoelectric

Rotational piezoelectric transducers work on the principle of plucking which only requires a relatively small rotation. The piezoelectric cantilever beams have to be bend and released, for this to be possible the compliant joint should minimally need to be able to facilitate the translation of the tip of the beam with some additional space to facilitate the release. Because piezoelectric material is usually brittle, this translation is marginal. After the cantilever is excited its amplitude decays and the system will start producing energy again after the following plucking. The required stroke is determined by the energy the proof mass should be able to accumulate from an arm swing before plucking. This energy is dependent on design parameters like the stiffness of the mechanism and amount of piezoelectric cantilevers that have to be plucked.

Stiffness

Apart from range of motion, stiffness is also an important design criterion. The working principle of a motion energy harvester is based on the inertial and gravitational forces acting on a proof mass. To increase the energy in this system the proof mass should be made as heavy as possible, there is however a limit to the weight of a proof mass imposed by design dimension and material choices. Because of this limited weight there is also a limited resistance the mechanism can impose on the proof mass to maintain functionality. This resistance is composed of electrical resistance from the transducer and mechanical resistance from the mechanism. When the proof mass is compliantly suspended the mechanism inherently imposes a stiffness to the system. This stiffness effectuates a buildup of force when the amplitude of the rotation of the proof mass

becomes bigger. At some point this force stops the rotation and flips it, creating an oscillation. By implementing the compliant rotational joints found in literature as an input for an energy harvester, this system becomes resonant.

III. Results

Rotational small scale energy harvesters can be divided into two categories: Large stroke motion input, which are electromagnetic and electrostatic generators. And short stroke motion input, which are piezoelectric generators based on a plucking principle. From literature, compliant rotational joints are found to have a wide variety of stroke lengths and stiffnesses. However, the compliant mechanisms considered always have a limited stroke which makes these systems oscillatory. Where most energy harvesters from literature are non-resonant, they should now be considered as resonant systems.
The design of a non-resonant compliant energy harvester would require a scalable extremely low- or zero-stiffness compliant rotational joint with large or even infinite stroke, this is not found in literature.

A. Large stroke harvesting

To be able to utilize a compliant joint as the input motion for an electromagnetic or electrostatic generator, large stroke compliant mechanisms have to be considered. This is seen in the calculation for maximum achievable power for rotational harvesters (Eq. 3) and from experimental results found in literature [16], [17]. Leaf spring compliant mechanisms, especially sophisticated leaf spring designs like the ones found in Fig. 4(p) and Fig. 4(q) are able to provide a large stroke well above arm swing input amplitude (30 degrees) and might be compatible with large stroke energy harvesters. The lower the stiffness of the mechanism, the larger the amplitude can become under human excitation conditions. Therefore it is favourable to have mechanisms as far in the top left of Fig. 5 as possible for large stroke harvesters. From this it can also be concluded that notch type flexures are not compatible for large stroke harvesting because of their relatively small range of motion and high stiffness.
Halim et. al. [28] and Zhang et. al. [32] explore the possibility to induce resonance at walking to significantly increase power production of a resonant rotational energy harvester. These mechanisms rely on an eccentric proof mass that is sprung by a coiled spring which allows for the eccentric mass to harness large amplitude motion (25 degree arm swing) and induces a resonant behaviour instead of non-resonant rotation seen in conventional rotational energy harvesters. The difference between power production of a resonant and a non-resonant rotational harvester is examined by Yeatman et. al. [10]. For a non-resonant rotating half disc with inertia

$$I = \frac{mR^2}{4} \tag{4}$$

where *m* denotes the total mass and R the proof mass radius, the maximum power (when parasitic damping is neglected) is found as:

$$Pmax = \frac{m\omega^3\Omega^2R^2}{16} \tag{5}$$

For the same rotating half disk which is sprung, creating a resonant system, the following maximum power is found:

$$Pmax = \frac{m\omega^3\Omega^2R^2}{32}Q \tag{6}$$

Where Q denotes the quality factor which is denoted as the ratio of angular kinetic energy to the energy lost to parasitic damping per radian. A Q of up to 24 is stated for a spring that allows full rotation under 30 degree amplitude excitations [10].
Tested under normal walking conditions, which are characterised by low frequency (1 Hz) and large amplitude (25 degree arm swing), the sprung eccentric electromagnetic harvester proposed by Halim et. al. is found to generate 6 times more power than its unsprung counterpart. Zhang et. al. and Rantz et. al. claim the average power to be increased by 25 percent for sprung harvesters with respect to conventional ones [32], [33].

Because compliant joints also introduce a stiffness it is an interesting objective to utilise this stiffness to obtain similar resonant behaviour at human input excitations like walking. The optimal stiffness that is implemented by Halim et. al. to exhibit this resonance during walking is however much lower than the stiffnesses of compliant mechanisms found in this paper, with a factor of roughly 20. The explanation for this is the extremely low input frequency from human motion [7]. The reduction in stiffness of compliant joints to achieve similar benefit from resonance is considered to be an interesting topic for further research. However, because this reduction would have to be significant, it is expect to be a difficult challenge.

B. Short stroke harvesting

When regarding piezoelectric energy harvesters there seems to be a compatibility with both large stroke and short stroke rotational compliant joints because a large stroke is not necessary to pluck a piezoelectric cantilever beam and induce frequency up-conversion. How small this stroke can become is determined by how much energy should be accumulated by the proof mass during large amplitude arm swing. The amount of required energy is determined by design parameters like the stiffness of the piezoelectric material and the magnetic strength of magnets used for plucking. Experiments done by Pillatsch et. al. [34] show the behaviour of the system when the kinetic energy of the proof mass is not enough to pluck the piezoelectric cantilever beam, making plucking impossible. In the case of this experiment the magnetic force of the plucking magnet is too high, showing the lowest excitation limit which can be used to create an optimal design.

Because this is a novel technique, and because it is hard to exactly model human movement, further research is required and experimental prototypes have to be made. Both notch- and leaf-type compliant mechanisms should be considered

when designing a piezoelectric plucked energy harvester.

An important finding on piezoelectric materials in energy harvesters that should be noted is their susceptibility to the number of performed cycles. It is found that when subjecting piezoelectric material to a large number of load cycles, it's key characteristics change. The most important one being it's resonance frequency due to stiffness reduction [35]. This effect is claimed to possibly be detrimental to energy harvesters and requires the further development of these materials to become a feasible option for energy harvesting.

C. Stiffness

To obtain resonance from a sprung rotational energy harvester a sufficiently low stiffness should be achieved. An indication for the required stiffness to achieve resonance from human input excitation can be obtained from the prototype tests done by Halim et. al. [28], where an optimal stiffness of around $1.3 * 10^{-4}$ Nm/rad is found. This stiffness is not obtained by compliant joints found in literature, which yields the conclusion that the direct implementation state-of-the-art compliant joints to obtain a resonant rotational energy harvester seems infeasible. Further research should be done on lowering the stiffness of these mechanisms or on the design of a new compliant rotational joint with sufficiently low stiffness, while maintaining the range of motion of current state-of-the-art compliant joints.

One of the strengths of compliant mechanisms is the high influence on stiffness by altering design choices like flexure length, shape and material, so the modification of current compliant joint designs like thinner or longer flexures should be investigated. Possibilities of stiffness reduction by implementing principles of the statically balanced near zero-stiffness mechanisms proposed by Morsch et. al. and Kuppens et. al. might provide an outcome for the low-stiffness requirement but are in need of further development to reduce size. In these systems buckled beams are used to create a negative stiffness in the direction of motion which result in a significantly lowered overall stiffness [29], [30].

For the determination of an ideal stiffness, particular harvester designs should be modeled. Input frequency, amplitude, transducer type and proof mass weight are among the things that determine what stiffness is desired from a mechanism and yield the optimal design parameters. To obtain enhanced efficiency from a sprung eccentric energy harvester the system should be tuned to have a resonant frequency at the most most common input frequency.

The strong dependence on specific input excitations poses a shortcoming in the state-of-the-art. Current literature on resonant rotational energy harvesters propose the implementation of a spring with linear spring stiffness [28], only making the mechanism susceptible to a narrow bandwidth of input excitations (frequency and amplitude). The implementation of a mechanism that has both low stiffness and that is susceptible to multiple input excitations could significantly benefit power generation and is considered to be a relevant topic for further research.

IV. Discussion

It is stated that a compliant rotational energy harvester will yield higher efficiency at it's natural frequency. However, human movement is characterised by irregular and fluctuating frequencies and the implementation of a compliant mechanism might narrow the operational bandwidth of the system. If the enhanced energy production at resonance frequency outweighs the narrowed bandwidth resulting in a higher energy production throughout the day is yet unknown and should be modeled or experimentally proven. As stated before, a solution could be the implementation of a system that resonates at multiple frequencies.

For a compliant resonant rotational harvester system to be created that resonates at human excitation input the stiffness of the compliant joints found in literature are still too high. The lowest reported stiffness, that of the flexure in Fig. 4 (p), is roughly a factor 20 higher than the stiffness reported by Halim et. al. that enhances power output during walking, which is a significant amount. Although the range of motion is found to be sufficient, the possibility to reduce stiffness will be crucial for the feasibility of a resonant compliant rotational energy harvester.

Most mechanisms reviewed by Farhadi et. al. [11] are already reviewed at a scale that is comparable to that of state-of-the-art wearables. Therefore their characteristics are directly compared with characteristics of harvesters found in literature. To validate if this comparison is justified models and/or prototypes should be made incorporating these mechanisms in harvester prototypes. This is however not considered to be within the scope of this review. The comparison with mechanisms found in literature that are of larger scale also requires an additional scalability analysis. The mechanism proposed by Spanoudakis et. al. [36], which can be found in section VI, shows a promising compatibility in range of motion with large stroke harvesters. However, due to it's scale, a direct comparison with other mechanisms and with required transducer input motion can not be made before performing a scalability analysis.

The required stroke length from a compliant mechanisms is deducted from the best suitable input motion for a specific transduction type. Even though this is based on design dimensions from existing prototypes, the exact values are still quite arbitrary and are mainly an indication of what type of stroke is most suitable: large stroke or short stroke. Where large stroke harvesters are considered to generate more power with increasing stroke, whereas short stroke harvesters are already able to generate their target power with a short stroke. Using this distinction, a categorisation of compliant joints found in literature can be made. However, the exact border between large stroke mechanisms and short stroke mechanisms is not clearly defined. Conclusions are made by looking at the extremes of both, for which the type of stroke is more obviously defined.

In this article an energy harvester is assumed to contain only one type of transduction. However, in literature, hybrid systems are also found [37]. The possible higher efficiency of these systems is thus not considered. It is however thought that an insight into the required range of motion and corresponding

compliant mechanism with regards to these hybrid systems can be obtained from the analysis in this paper. Furthermore, the article does not go in depth on the principle of electrostatic transduction because it is found to behave similar to electromagnetic induction as far as input motion.

V. Conclusion

Literature proposes many designs to convert the kinetic energy from human movement into electricity by using rotational energy harvesting, implementing either electromagnetic, electrostatic or piezoelectric transduction. The most prominent design is a rotational energy harvester. Capturing this motion using a compliant joint might benefit the system from general advantages of compliant mechanisms like reduction of friction and wear. The characteristics of compliant joints found in literature are evaluated from which the compatibility with various transduction methods is concluded. Electromagnetic and electrostatic transducers are found to be optimal at large stroke lengths, which can be provided by leaf spring compliant mechanisms. Piezoelectric transducers implementing a plucking principle require less stroke for which both notch type and leafspring compliant mechanisms might be compatible. The implementation of a compliant joint introduces a stiffness to the system. Sprung rotational energy harvesters are found to significantly benefit the power output of the system through resonance, when the optimal stiffness is chosen for a specific human input excitation. This optimal stiffness is however found to be significantly lower than the stiffness introduced by the lowest stiffness compliant joint. Future research should be done on the reduction of stiffness for a compliant joint to create a resonating compliant rotational energy harvester under human input excitations. Furthermore, this research can be elaborated upon by researching the possibility to create a system that experiences resonance at multiple input excitations. Creating a system which is susceptible to multiple human activities (walking, running, etc.).

Acknowledgment

I would like to thank Werner van de Sande, Gerard Dunning and Joep Meij for their supervision and guidance.

References

[1] Paul D. Mitcheson, Eric M. Yeatman, G. Kondala Rao, Andrew S. Holmes, and Tim C. Green. Energy harvesting from human and machine motion for wireless electronic devices. *Proceedings of the IEEE*, 96:1457–1486, 2008.

[2] Hailing Fu, Xutao Mei, Daniil Yurchenko, Shengxi Zhou, Stephanos Theodossiades, Kimihiko Nakano, and Eric M. Yeatman. Rotational energy harvesting for self-powered sensing, 5 2021.

[3] Longhan Xie, Carmen G. Menet, Ho Ching, and Ruxu Du. The automatic winding device of a mechanical watch movement and its application in energy harvesting. *Journal of Mechanical Design, Transactions of the ASME*, 131:0710051–0710057, 7 2009.

[4] Nidal M. Turab, Hamza Abu Owida, Jamal I. Al-Nabulsi, and Mwaffaq Abu-Alhaija. Recent techniques for harvesting energy from the human body, 2022.

[5] Shadrach Joseph Roundy. Energy scavenging for wireless sensor nodes with a focus on vibration to electricity conversion, 1996.

[6] Larry L. Howell. Compliant mechanisms, 2013.

[7] Erik K Antonsson and Robert W Mann. The frequency content of gait, 1985.

[8] Dean M. Karantonis, Michael R. Narayanan, Merryn Mathie, Nigel H. Lovell, and Branko G. Celler. Implementation of a real-time human movement classifier using a triaxial accelerometer for ambulatory monitoring. *IEEE Transactions on Information Technology in Biomedicine*, 10:156–167, 1 2006.

[9] Aiden Doherty, Dan Jackson, Nils Hammerla, Thomas Plötz, Patrick Olivier, Malcolm H. Granat, Tom White, Vincent T. Van Hees, Michael I. Trenell, Christoper G. Owen, Stephen J. Preece, Rob Gillions, Simon Sheard, Tim Peakman, Soren Brage, and Nicholas J. Wareham. Large scale population assessment of physical activity using wrist worn accelerometers: The uk biobank study. *PLoS ONE*, 12, 2 2017.

[10] E. M. Yeatman. Energy harvesting from motion using rotating and gyroscopic proof masses. *Proceedings of the Institution of Mechanical Engineers, Part C: Journal of Mechanical Engineering Science*, 222:27–36, 1 2008.

[11] D. Farhadi Machekposhti, N. Tolou, and J. L. Herder. A review on compliant joints and rigid-body constant velocity universal joints toward the design of compliant homokinetic couplings, 2015.

[12] Salman Khalid, Izaz Raouf, Asif Khan, Nayeon Kim, and Heung Soo Kim. A review of human-powered energy harvesting for smart electronics: Recent progress and challenges, 8 2019.

[13] C B Williams, C Shearwood, M A Harradine, P H Mellor, T S Birch, and R B Yates. Development of an electromagnetic micro-generator.

[14] Hailing Fu and Eric M. Yeatman. Comparison and scaling effects of rotational micro-generators using electromagnetic and piezoelectric transduction. *Energy Technology*, 6:2220–2231, 11 2018.

[15] Dragan Dinulovic, Michael Brooks, Martin Haug, and Tomislav Petrovic. Rotational electromagnetic energy harvesting system. volume 75, pages 1244–1251. Elsevier B.V., 2015.

[16] Mehdi Niroomand and Hamid Reza Foroughi. A rotary electromagnetic microgenerator for energy harvesting from human motions. *Journal of Applied Research and Technology*, 14:259–267, 8 2016.

[17] Huicong Liu, Cheng Hou, Jiahong Lin, Yunfei Li, Qiongfeng Shi, Tao Chen, Lining Sun, and Chengkuo Lee. A non-resonant rotational electromagnetic energy harvester for low-frequency and irregular human motion. *Applied Physics Letters*, 113, 11 2018.

[18] P D Mitcheson, T Sterken, C He, M Kiziroglou, E M Yeatman, and R Puers. Electrostatic microgenerators.

[19] Kwan Chi Kao. 5 - electrets. In Kwan Chi Kao,

editor, *Dielectric Phenomena in Solids*, pages 283–326. Academic Press, San Diego, 2004.

[20] Justin Boland, Yuan-Heng Chao, Yuji Suzuki, and Y C Tai. Micro electret power generator.

[21] J. Nakano, K. Komori, Y. Hattori, and Y. Suzuki. Mems rotational electret energy harvester for human motion. volume 660. Institute of Physics Publishing, 12 2015.

[22] Mingzhao Bi, Shiwen Wang, Xiaofeng Wang, and Xiongying Ye. Freestanding-electret rotary generator at an average conversion efficiency of 56 *Nano Energy*, 41:434–442, 11 2017.

[23] Abdul Aabid, Md Abdul Raheman, Yasser E. Ibrahim, Asraar Anjum, Meftah Hrairi, Bisma Parveez, Nagma Parveen, and Jalal Mohammed Zayan. A systematic review of piezoelectric materials and energy harvesters for industrial applications, 6 2021.

[24] Pit Pillatsch, Eric M. Yeatman, and Andrew S. Holmes. A piezoelectric frequency up-converting energy harvester with rotating proof mass for human body applications. *Sensors and Actuators, A: Physical*, 206:178–185, 2 2014.

[25] Yipeng Wu, Jinhao Qiu, Fumio Kojima, Hongli Ji, Weitai Xie, and Shengpeng Zhou. Design methodology of a frequency up-converting energy harvester based on dual-cantilever and pendulum structures. *AIP Advances*, 9, 4 2019.

[26] Apa) Farhadi Machekposhti, D L Herder, J Semon, and G Tolou. Swiss watch featuring dutch precision. mikroniek: vakblad voor precisie-technologie, 2018.

[27] Elke Warmerdam, Robbin Romijnders, Julius Welzel, Clint Hansen, Gerhard Schmidt, and Walter Maetzler. Quantification of arm swing during walking in healthy adults and parkinson's disease patients: Wearable sensor-based algorithm development and validation. *Sensors (Switzerland)*, 20:1–12, 10 2020.

[28] M. A. Halim, R. Rantz, Q. Zhang, L. Gu, K. Yang, and S. Roundy. An electromagnetic rotational energy harvester using sprung eccentric rotor, driven by pseudo-walking motion. *Applied Energy*, 217:66–74, 5 2018.

[29] Femke M. Morsch and Just L. Herder. Design of a generic zero stiffness compliant joint. volume 2, pages 427–435, 2010.

[30] P. R. Kuppens, M. A. Bessa, J. L. Herder, and J. B. Hopkins. Monolithic binary stiffness building blocks for mechanical digital machines. *Extreme Mechanics Letters*, 42, 1 2021.

[31] Ruxu Du and Longhan Xie. *The Mechanics of Mechanical Watches and Clocks*, volume 21. Springer Berlin Heidelberg, 2013.

[32] Institute of Electrical, Electronics Engineers, and IEEE Sensors Council. *IEEE SENSORS 2016 : Orlando, Florida, USA, October 30-November 2, 2016 : 2006 proceedings papers*.

[33] R. Rantz, M. A. Halim, T. Xue, Q. Zhang, L. Gu, K. Yang, and S. Roundy. Architectures for wrist-worn energy harvesting. *Smart Materials and Structures*, 27, 3 2018.

[34] P. Pillatsch, E. M. Yeatman, and A. S. Holmes. A wearable piezoelectric rotational energy harvester. 2013.

[35] P. Pillatsch, N. Shashoua, A. S. Holmes, E. M. Yeatman, and P. K. Wright. Degradation of piezoelectric materials for energy harvesting applications. volume 557. Institute of Physics Publishing, 2014.

[36] Peter Spanoudakis, Lionel Kiener, Florent Cosandier, Philippe Schwab, Laurent Giriens, Johan Kruis, Daniel Grivon, Georgia Psoni, Christos Vrettos, and Nabil Bencheikh. Large angle flexure pivot development for future science payloads.

[37] Miles Larkin and Yonas Tadesse. Hm-eh-rt: Hybrid multimodal energy harvesting from rotational and translational motions. *International Journal of Smart and Nano Materials*, 4:257–285, 12 2013.

[38] J A Haringx. The cross-spring pivot as a constructional element.

[39] Stuart Smith. *Flexures: Elements of Elastic Mechanisms*. 08 2000.

[40] *Novel Flexible Pivot With Large Angular Range and Small Center Shift to be Integrated Into a Bio-Inspired Robotic Hand*, volume ASME 2010 Conference on Smart Materials, Adaptive Structures and Intelligent Systems, Volume 2 of *Smart Materials, Adaptive Structures and Intelligent Systems*, 09 2010.

[41] Pei Xu, Yu Jingjun, Zong Guanghua, and Bi Shusheng. The Stiffness Model of Leaf-Type Isosceles-Trapezoidal Flexural Pivots. *Journal of Mechanical Design*, 130(8), 07 2008. 082303.

[42] X Pei and J Yu. Adlif: A new large-displacement beam-based flexure joint. *Mechanical Sciences*, 2, 08 2011.

[43] Brian P. Trease, Yong-Mo Moon, and Sridhar Kota. Design of Large-Displacement Compliant Joints. *Journal of Mechanical Design*, 127(4):788–798, 11 2004.

[44] Jingjun Yu. A new large-stroke compliant joint micro/nano positioner design based on compliant building blocks metamaterial view project tuned mass damper view project a new large-stroke compliant joint micro/nano positioner design based on compliant building blocks, 2009.

[45] Robert M. Fowler, Alex Maselli, Pieter Pluimers, Spencer P. Magleby, and Larry L. Howell. Flex-16: A large-displacement monolithic compliant rotational hinge. *Mechanism and Machine Theory*, 82:203–217, 2014.

[46] Jason Dearden, Clayton Grames, Jason Orr, Brian D. Jensen, Spencer P. Magleby, and Larry L. Howell. Cylindrical cross-axis flexural pivots. *Precision Engineering*, 51:604–613, 1 2018.

[47] Lifang Qiu, Yuansong Liu, Yue Yu, and Yuntian Brian Bai. Design and stiffness analysis of a pitch-varying folded flexure hinge (pffh). *Mechanism and Machine Theory*, 157, 3 2021.

VI. Supplementary materials literature review

A. Maximum deflection calculation code

```
clc
clear all
close all

syms notch
syms leaf
syms plus
syms zero
syms minus
syms a b c f g h i j k l m o p q

%% mechanism points
Name = [a b c f g h i j k l m o p q];
Stiffness = [6.481 0.112 23.342 0.0079 0.0315 0.0078 0.094 0.047 0.021 0.0941 0.126
    0.0057 0.0027 0.311];
RoM = [0.113 0.06 0.03 1.676 0.419 0.838 0.173 0.346 0.35 0.558 0.267 1.4 2.55 1.57];
Size = [plus plus plus zero plus zero plus zero zero minus minus minus zero zero];
Type = [notch notch notch leaf leaf leaf leaf leaf leaf leaf leaf leaf leaf leaf];

%% Deflection per stiffness calculation

m = 10.7*10^-3; %eccentric mass [kg]
L = 0.6; %arm length [m]
theta = 25; %arm swing angle [deg]
A = 2*pi*L*(theta/360); % arc length/amplitude [m]
f1 = 1; %arm swing frequency during walking (Hz)
f2 = 2; %arm swing frequency during runing (Hz)
omega1 = 2*pi*f1; %angular frequency during walking (rad/s)
omega2 = 2*pi*f2; %angular frequency during running (rad/s)
a1 = (omega1^2)*A; %maximum acceleration [m/s^2]
a2 = (omega2^2)*A; %maximum acceleration [m/s^2]
F1 = m*a1; %maximum force from swing during walking [N]
F2 = m*a2; %maximum force from swing during running [N]
l = 10*10^-3; %eccentic length [m]
M1 = F1*l; %moment durnig walking [Nm]
M2 = F2*l; %moment durnig running [Nm]
k = linspace(10^-3,10^2,1000000); %rotational stiffness sweep [Nm/rad]
deflection1 = 2*(M1./k); %deflection during walking [rad]
deflection2 = 2*(M2./k); %deflection during running [rad]

%% Plot
plot(deflection1,k)
hold on
plot(deflection2,k)
hold on
scatter(Stiffness,RoM,'.','black')
hold on
grid on
set(gca,'xscale','log','FontSize',15)
xlim([(10^-3) (10^2)])
ylim([0 3])
xlabel('Rotational Stiffness [Nm/rad]')
ylabel('Range of Motion [rad]')
text(Stiffness(1),RoM(1),'  a','Color','[0.4660 0.6740 0.1880]','FontSize',20)
```

```
text(Stiffness(2),RoM(2),'  b','Color','[0.4660 0.6740 0.1880]','FontSize',20)
text(Stiffness(3),RoM(3),'  c','Color','[0.4660 0.6740 0.1880]','FontSize',20)
text(Stiffness(4),RoM(4),'  f','Color','b','FontSize',20)
text(Stiffness(5),RoM(5),'  g','Color','[0.4660 0.6740 0.1880]','FontSize',20)
text(Stiffness(6),RoM(6),'  h','Color','b','FontSize',20)
text(Stiffness(7),RoM(7),'  i','Color','[0.4660 0.6740 0.1880]','FontSize',20)
text(Stiffness(8),RoM(8),'  j','Color','b','FontSize',20)
text(Stiffness(9),RoM(9),'  k','Color','b','FontSize',20)
text(Stiffness(10),RoM(10),'  l','Color','r','FontSize',20)
text(Stiffness(11),RoM(11),'  m','Color','r','FontSize',20)
text(Stiffness(12),RoM(12),'  o','Color','r','FontSize',20)
text(Stiffness(13),RoM(13),'  p','Color','[0.4660 0.6740 0.1880]','FontSize',20)
text(Stiffness(14),RoM(14),'  q','Color','[0.4660 0.6740 0.1880]','FontSize',20)
legend('Deflection at walking (1 Hz)','Deflection at running (2 Hz)','Compliant Joint')
```

B. Bundled compliant rotational joints

Compliant rotational mechanism	Type	Range of motion (rad)	Rotational stiffness (Nm/rad)	Size
Fig. 4(a)	notch type	0.113	6.481	+
Fig. 4(b)	notch type	0.06	0.112	+
Fig. 4(c)	notch type	0.03	23.342	+
Haringx et. al. [38] Fig. 4(f)	leaf spring	1.676	0.0079	0
Smith et. al. [39] Fig. 4(g)	leaf spring	0.419	0.0315	+
Martin et. al. [40] Fig. 4(h)	leaf spring	0.838	0.0078	0
Xu et. al. [41] Fig. 4(i)	leaf spring	0.173	0.094	+
Pei et. al. [42] Fig. 4(j)	leaf spring	0.346	0.047	0
Pei et. al. [42] Fig. 4(k)	leaf spring	0.35	0.021	0
Trease et. al. [43] Fig. 4(l)	leaf spring	0.558	0.0941	-
Trease et. al. [43] Fig. 4(m)	leaf spring	0.267	0.126	-
Trease et. al. [43] Fig. 4(o)	leaf spring	1.4	0.0057	-
Yu et. al. [44] Fig. 4(p)	leaf spring	2.55	0.0027	+
Fowler et. al. [45] Fig. 4(q)	leaf spring	1.57	0.311	+
Spanoudakis et. al. [36]	leaf spring	3.14	0.08 - 0.34	0
Dearden et. al. [46]	leaf spring	2.97	0.0057	0
Qiu et. al. [47]	folded spring	2.96	0.029-0.061	+

TABLE II. FLEXURE TYPE, RANGE OF MOTION, STIFFNESS AND SIZE OF COMPLIANT MECHANISMS FOUND IN LITERATURE.

A + corresponds to a size which is considered to be implementable at harvester scale without losing function, a 0 corresponds to scalability being feasible but with possible loss in functionality and a - corresponds to implementation being infeasible because of size.

APPENDIX B
SIMULATION

The main method used to obtain an understanding of the dynamics of a sprung rotational energy harvester was through simulation of the system. Simscape Multibody was used to create a 'pseudo walking' simulation which could be physically recreated within a realistic time frame, the schematic block diagram is shown in Fig. 19. The simulation gives excellent adjustability to study different harvester geometries paired with varying stiffnesses and excitation inputs. The simulation is composed of a stiff 0.6 meter long beam with a rotor connected to the end (highlighted in purple). Simulating an arm wearing a wearable with a rotational energy harvester under walking excitation. The simulation allows for the actuation of the (shoulder) joint about which the arm rotates for which frequency and amplitude can be adjusted (highlighted in green). Viscous damping of the rotor was applied in the adjustable parameters of its joint. Furthermore a Coulomb damping torque was added (highlighted in red). Viscous- and Coulomb damping were determined from measurements of the Seiko Kinetic watch reported by Xue et al. [15]. The output was defined as the angle of the rotor (highlighted in blue) which is calculated per simulation time step of 0.0001 seconds. This simulation was run twice simultaneously where one of the simulations has the addition of a stiffness term to the rotor (highlighted in yellow) which was defined in a separate Matlab function. Simulations were performed over a range of arm swing amplitudes while keeping the arm swing frequency constant. The generated power was calculated by deriving the angular velocity of the rotor and multiplying it by the electrical damping in the system. The average power was calculated at each excitation input by taking the integral of the power over time and dividing it by the total simulation time. According to Eq. 24.

$$P_{avg} = \frac{1}{T}\int_0^T c_e \dot{\theta} dt \tag{24}$$

To obtain a performance metric for the system over the entire range of excitation inputs the 'daily average power' was determined. This was determined by averaging the average powers of the excitation inputs considered as walking slow and averaging the average powers of the excitation inputs considered as walking fast. These were multiplied by the minutes spend in the corresponding activity divided by the total minutes spend walking per day. The calculations can be found in the Matlab code added to the end of appendix B. Chat GPT was used for some parts of the code.

A. *Stiffness*

The simulated stiffness, highlighted in yellow in Fig. 19, is interpreted from a Matlab function. The simulated angular displacement of the rotor is fed to a function which calculates a corresponding torque, denoted as function output y, based on simulated spring stiffness. In the case of a simulation with a spring with infinite range of motion the stiffness function is denoted as:

```
function y = StiffnessSeiko(x)
%% Linear stiffness
a = 1.8286e-04; %Stiffness coefficient [N.m/rad]
y = sign(x)*(a*abs(x));
end
```

When the flexure mechanism is simulated a physical stop is incorporated. Measurements of the produced flexure mechanism are used to make a continuous fit which approximates the stiffness profile of the spring. Resulting in a linear increase in torque up to the point where the physical stop is met from where the curve exponentially increases. For the simulation of the flexure mechanism the stiffness function is denoted as:

```
function y = NonlinearStiffness(x)
%% Exponential fit (movable stop)
a = 0.00051; %linear stiffness part
b = 45; %exponential increase
c = 10^-28.5; %stop location
y = sign(x)*(a*abs(x) + c*exp(b*abs(x)));
end
```

The resulting stiffness profile is shown in Fig. 17

B. *Damping*

The simulation accounts for viscous damping, dependant on velocity, comprised of a mechanical and an electrical term. Furthermore the system accounts for Coulomb damping, consisting of a constant damping term independent on velocity. To

account for Coulomb damping a constant torque in the opposite direction of rotation is introduced and highlighted in red in Fig. 19. The Coulomb damping is found to have a large influence on the system's susceptibility to move under low energy input excitation. Both mechanical and electrical damping are linear terms and are summed up to create one linear viscous damping term. Simscape Multibody allows for the introduction of such a damping term within the joint connecting the arm and the rotor. A visualisation of the simulated total damping of the Seiko Kinetic watch can be found in Fig. 18, in which coulomb damping amounts to $2.2 \cdot 10^{-5}$ Nm and total viscous damping to $5.3 \cdot 10^{-7}$ Nms.

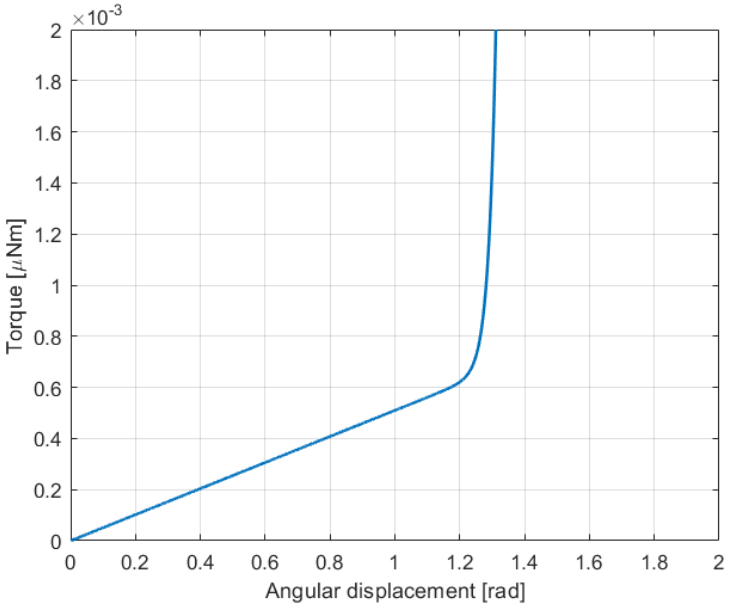

Fig. 17: Stiffness profile of the flexure mechanism.

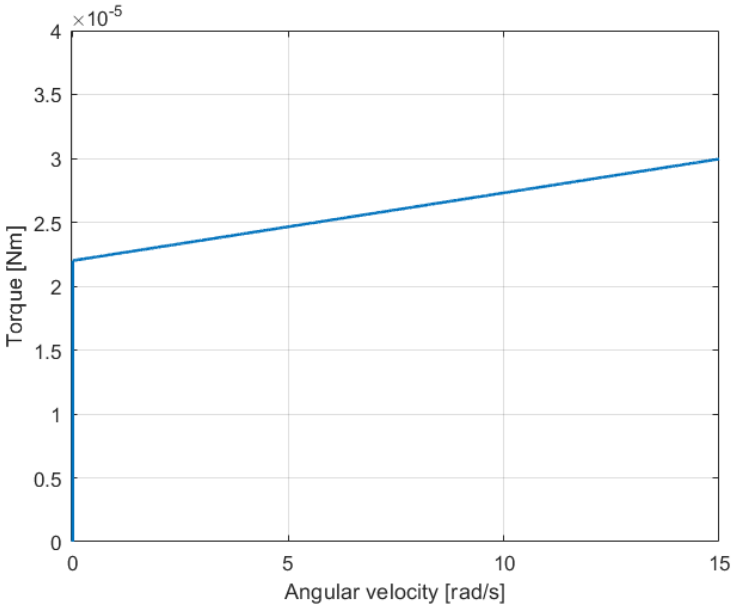

Fig. 18: Damping profile of the Seiko Kinetic watch.

C. Model representation

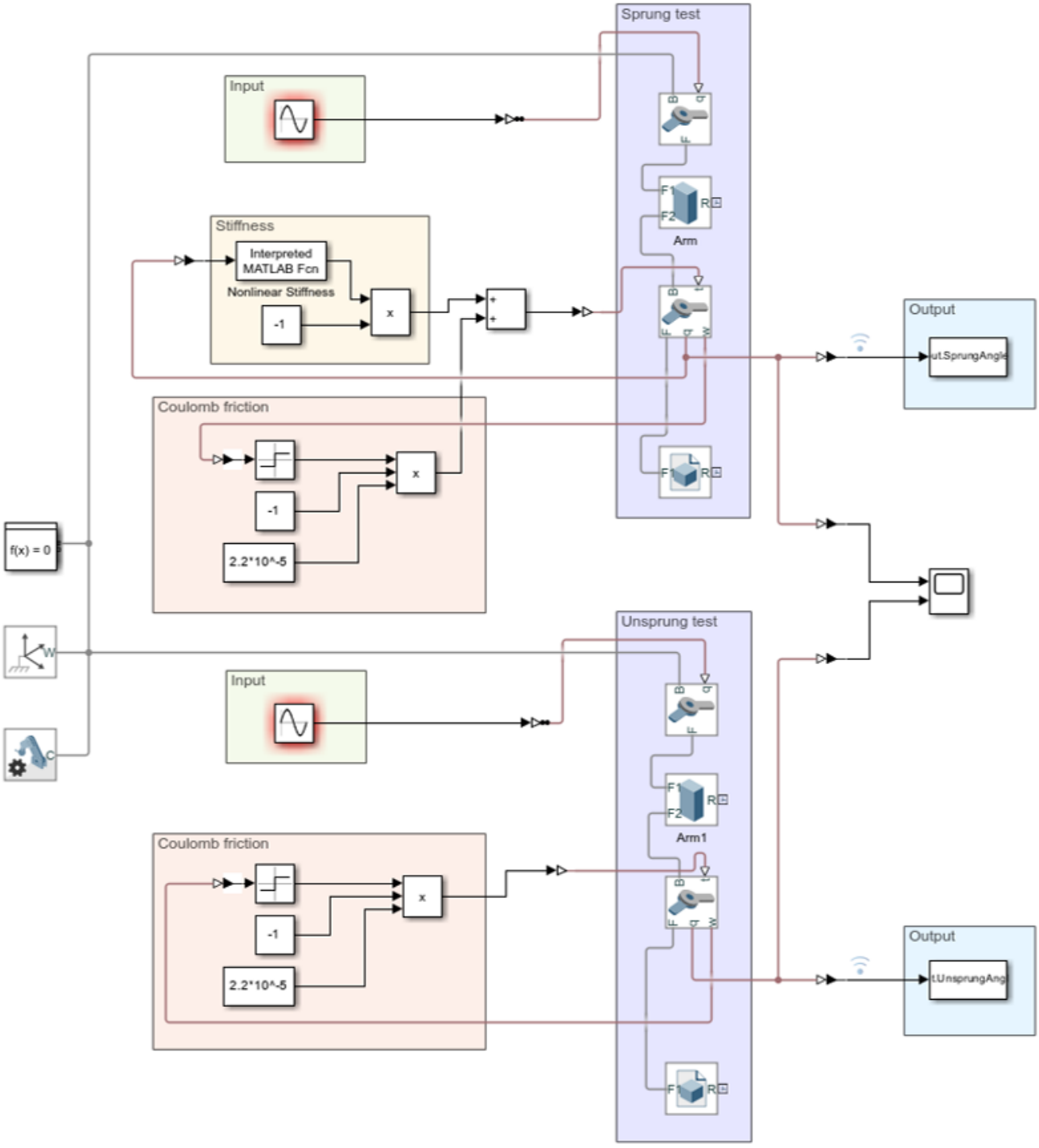

Fig. 19: Simulink model for the simulation of the energy harvester found in the Seiko Kinetic watch under pseudo walking excitation.

D. Simulation results

Results of the simulation of the rotor angle over time of a Seiko Kinetic watch under the excitation of a pseudo arm swing with amplitude of 20 degrees and frequency of 0.9 hertz are shown in Fig. 20. Simulation of the flexure mechanism at 0.9 Hertz arm swing frequency were performed at arm swing amplitudes of 5, 10 and 22 degrees, of which the results are shown in Fig. 21, 22 and 23 respectively.

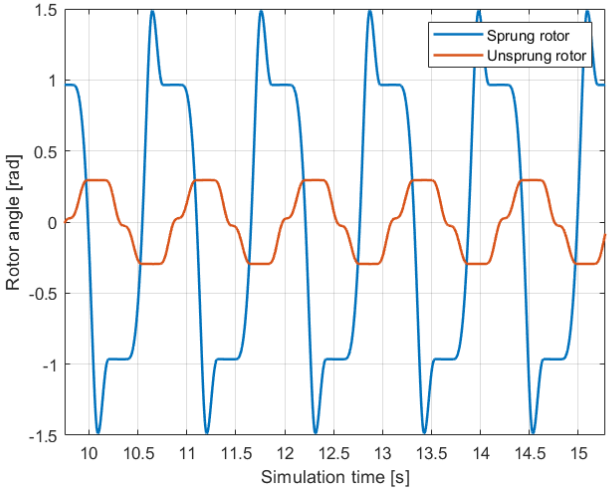

Fig. 20: Simulation of the rotor angle over time of a Seiko Kinetic subject to a pseudo arm swing with an amplitude of 20 degrees and frequency of 0.9 hertz.

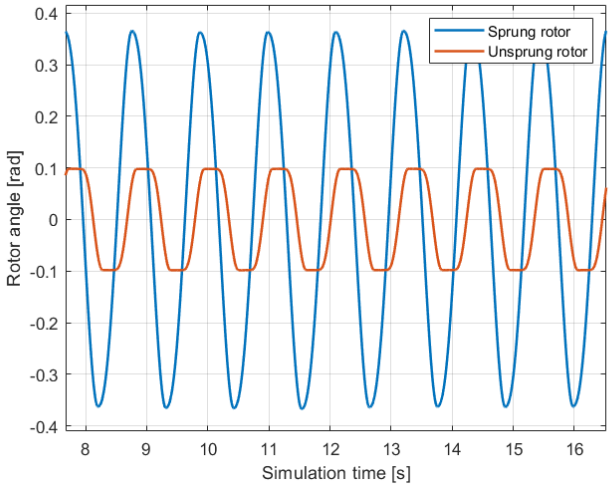

Fig. 21: Simulation of the rotor angle over time of the physical test subject to a pseudo arm swing with an amplitude of 5 degrees and frequency of 0.9 hertz.

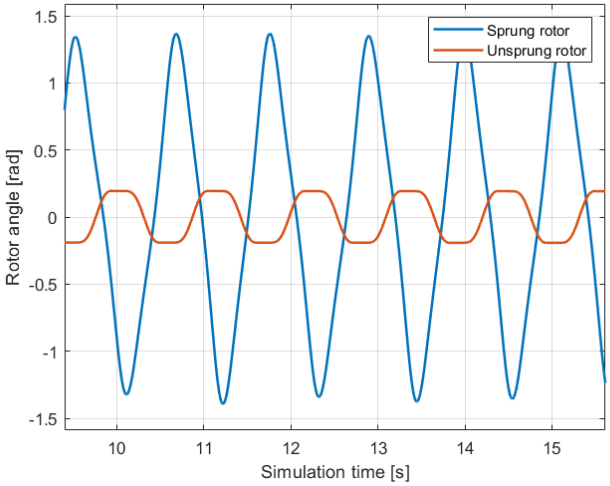

Fig. 22: Simulation of the rotor angle over time of the physical test subject to a pseudo arm swing with an amplitude of 10 degrees and frequency of 0.9 hertz.

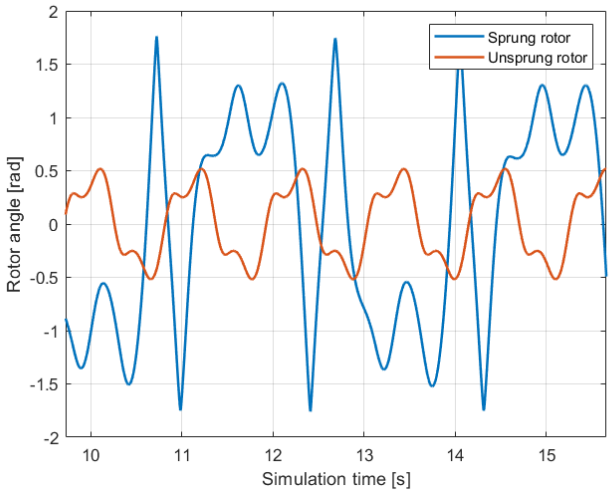

Fig. 23: Simulation of the rotor angle over time of the physical test subject to a pseudo arm swing with an amplitude of 22 degrees and frequency of 0.9 hertz.

E. Matlab simulation code for the Seiko Kinetic

```
clear all
close all
clc

open_system("PendulumTest3Seiko")
set_param('PendulumTest3Seiko/Stiffness','Value','Stiffness')
set_param('PendulumTest3Seiko/Sine','Frequency','Frequency1')
set_param('PendulumTest3Seiko/Sine','Amplitude','Amplitude')

%% Frequency
Frequency = 0.9; %Arm swing frequency in Hertz
%% Amplitude
AmplitudeSweep = linspace(0.2,0.435,15); %Sweep of arm swing amplitudes in rad
%% Frequency input
for i = 1:length(FrequencySweep)
    simIn(i) = Simulink.SimulationInput('PendulumTest3Seiko');
    simIn(i) = setVariable(simIn(i),'Frequency',Frequency);
end
%% Amplitude input
for i = 1:length(AmplitudeSweep)
    simIn(i) = Simulink.SimulationInput('PendulumTest3Seiko');
    simIn(i) = setVariable(simIn(i),'Amplitude',AmplitudeSweep(i));
end
simOutputs = sim(simIn);
%% Set up zero matrices for displacement, velocity and power
SprungAngles = zeros(length(simOutputs(1).SprungAngle.Time),length(simOutputs)+1);
UnsprungAngles = zeros(length(simOutputs(1).UnsprungAngle.Time),length(simOutputs)+1);
GradSprung = zeros(length(simOutputs(1).SprungAngle.Time),length(simOutputs)+1);
GradUnsprung = zeros(length(simOutputs(1).SprungAngle.Time),length(simOutputs)+1);
SprungVel = zeros(length(GradSprung(:,1)),length(simOutputs));
UnsprungVel = zeros(length(GradUnsprung(:,1)),length(simOutputs));
PowerSprung = zeros(length(GradSprung(:,1)),length(simOutputs));
PowerUnsprung = zeros(length(GradUnsprung(:,1)),length(simOutputs));

%% Electrical Damping of Generator implemented in Seiko watches
Ce = 4*10^-7; %Electrical damping coefficient in Nms/rad

%% Determine power from velocity
for i = 1:length(simOutputs)
    SprungAngles(:,1) = simOutputs(1).SprungAngle.Time; %Load time from simulation
        output
    UnsprungAngles(:,1) = simOutputs(1).UnsprungAngle.Time;
    SprungAngles(:,i+1) = simOutputs(i).SprungAngle.Data; %Load data from simulation
        output
    UnsprungAngles(:,i+1) = simOutputs(i).UnsprungAngle.Data;
    GradSprung(:,1) = gradient(simOutputs(1).SprungAngle.Time); %Timestep
    GradUnsprung(:,1) = gradient(simOutputs(1).UnsprungAngle.Time);
    GradSprung(:,i+1) = gradient(simOutputs(i).SprungAngle.Data); %Gradient of angle
    GradUnsprung(:,i+1) = gradient(simOutputs(i).UnsprungAngle.Data);
    SprungVel(:,i) = GradSprung(:,i+1)./GradSprung(:,1); %Angular velocity per time
        step w = dtheta / dt
    UnsprungVel(:,i) = GradUnsprung(:,i+1)./GradUnsprung(:,1);
    PowerSprung(:,i) = 0.5 * Ce * (SprungVel(:,i).^2) .* GradSprung(:,1); %Power from
        electrical damping and velocity per time step
    PowerUnsprung(:,i) = 0.5 * Ce * (UnsprungVel(:,i).^2) .* GradUnsprung(:,1);
end
```

```
%% Determine total travelled angle and total power
TravelledSprung = sum(abs(GradSprung)); %Total travelled angle
TravelledUnsprung = sum(abs(GradUnsprung));
TotalPowerSprung = sum(PowerSprung); %Total power
TotalPowerUnsprung = sum(PowerUnsprung);

%% Determine average power and daily average power
AveragePowerSprung = TotalPowerSprung/30; %Average power
AveragePowerUnsprung = TotalPowerUnsprung/30;
WalkingSlow = find(AmplitudeSweep >= 0.08 & AmplitudeSweep <= 0.27 ); %Define amplitude
    corresponding to slow walking
WalkingFast = find(AmplitudeSweep >= 0.27 & AmplitudeSweep <= 0.47 ); %Define amplitude
    corresponding to fast walking
SlowPowerSprung = sum(AveragePowerSprung(WalkingSlow))/length(AveragePowerSprung(
   WalkingSlow));
FastPowerSprung = sum(AveragePowerSprung(WalkingFast))/length(AveragePowerSprung(
   WalkingFast));
SlowPowerUnsprung = sum(AveragePowerUnsprung(WalkingSlow))/length(AveragePowerUnsprung(
   WalkingSlow));
FastPowerUnsprung = sum(AveragePowerUnsprung(WalkingFast))/length(AveragePowerUnsprung(
   WalkingFast));
DailyAverageSprung = SlowPowerSprung*(19.48/(55.07+19.48)) + FastPowerSprung
   *(55.07/(55.07+19.48)); %Daily average power
DailyAverageUnsprung = SlowPowerUnsprung*(19.48/(55.07+19.48)) + FastPowerUnsprung
   *(55.07/(55.07+19.48));

%% Plot
figure()
plot(AmplitudeSweep,AveragePowerSprung*1000000,'LineWidth',1.5)
hold on
plot(AmplitudeSweep,AveragePowerUnsprung*1000000,'LineWidth',1.5)
xlabel("Amplitude [rad]")
ylabel("Average power [microW]")
title("Average power per arm swing amplitude")
grid on
xticks(0.08:0.05:0.435);
xlim([0.08 0.435])
yticks(0:4:60);
ylim([0 60]);
% text(0.1,60,sprintf('DailyAverageSprung=%f',DailyAverageSprung))
hold on
slow = area([0.08 0.262], [300 300],'FaceColor','r','FaceAlpha',0.1,'EdgeAlpha',0.2);
hold on
fast = area([0.262 0.4363],[300 300],'FaceColor','b','FaceAlpha',0.1,'EdgeAlpha',0.2);
hold on
legend('Sprung','Unsprung','Walking slow','Walking fast')
```

APPENDIX C
FLEXURE MECHANISM

A. Resonant design

Yeatman et al. [10] proposes the design of a resonant oscillating rotational harvester and claims a significant potential increase in average power. Following this, the initial objective in the design of a flexure mechanism was the creation of a resonant system under walking excitation to enhance performance. An attempt was made to design a mechanism which was susceptible to multiple low frequency inputs, to increase potential over the entire range of walking excitation. For this, multiple designs incorporating two proof masses were created and a modal analysis was performed, see Tab. VIII. To achieve multiple sufficiently low eigenmodes it was found that the total mass had to be relatively high, see Tab. VII. Furthermore, multiple proof masses require a non planar design at the scale of a watch to allow for flexures with sufficient length to facilitate a sufficiently low stiffness. The objective to create a planar design incentivised the research to focus on maximisation of operational range rather than resonance.

Design number	**1st eigenfrequency [Hz]**	**2nd eigenfrequency [Hz]**	**Total mass [g]**
1	0.812	7.7	30
2	0.99	8.55	15
3	0.96	6.84	19
4	0.83	3.29	29
5	0.787	2.99	28

TABLE VII: Analysis of eigenfrequencies of initial resonant designs, performed in SolidWorks.

B. Non-resonant design

Through simulations it was found that when stiffness is sufficiently low, a system could be created that has increased harvesting potential over a large range of excitation inputs without utilizing resonance. The added stiffness allows for the rotor to flip at a certain excitation input, after which this flipping behaviour enhances power output over the entire operational range. Yu et al. [17] addressed a method to design a compliant rotational joint for large operational range, based the principle of multiple leaf springs. Fig. 24 shows a large-stroke design composed of three 'building blocks' of multiple leaf flexures connected in series via intermediate bodies. By connecting multiple relatively long leaf flexures in series a low resultant rotational stiffness is obtained. A flexure was designed based on the design shown in Fig. 24. A rotor suspended by a rotational bearing is sprung using two modules of leaf flexures connected in series. Attaching to the rotor on one end and the the ground on the other end. The design is shown in Fig. 25. The design allows for the rotor to harness energy from kinetic motion and directly transfer it to the centre axle. While the flexures introduce a rotational stiffness to enhance the system's performance.

C. Analysis, manufacturing and measurements

The next step in the design of the sprung rotational energy harvester shown in Fig. 25 was analysis, prototyping and measurement. Separate from the research in this paper, Flexous initiated a study on scaling down and implementing the design. At the time of writing this study, the research is still in progress. However, a finite element model is completed by Alden Yellowhorse that was used to simulate the mechanism in this study. The rotation of the mechanism was simulated at increasingly higher moment loads, the results of which can be found in Tab. IX and Fig. 26. For the manufacturing of the flexure elements of the prototype a specialised tool was designed and 3D-printed. The tool allows for the bending of a 3mm wide strip of 1.4310 stainless steel at specific lengths. After inserting the steel strip the tool was used to manually bend the steel strip over a steel plate. The bending tool can be seen in Fig. 27. The rotor and a mount for the flexures were 3D-printed after which the flexures were glued into slits. The prototype is shown in Fig. 28 in the natural, partially deformed and maximally deformed position. The bolts mounted to the rotor are used as weights and can be changed to achieve a different rotor mass. This feature was implemented to be able to tune the mass based on the measured flexure stiffness. When the eventual stiffness was determined the mass of the rotor was altered to obtain desired system characteristics. After manufacturing, the flexure mechanism was characterised by measuring torque against deflection using a rheometer. The test set-up can be found in Fig. 29. Stiffness was measured over the entire operational range three times in both the clockwise and counterclockwise direction of which the data can be found in Fig. 30.

Design	1st mode sideview	1st mode	2nd mode
1	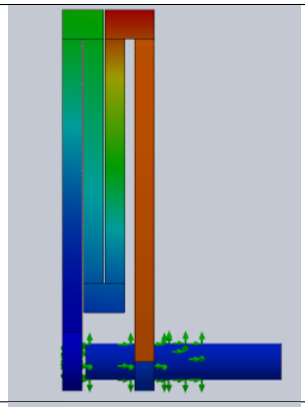	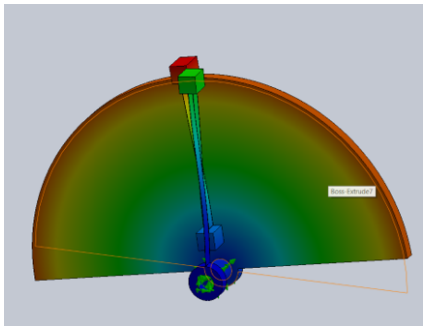	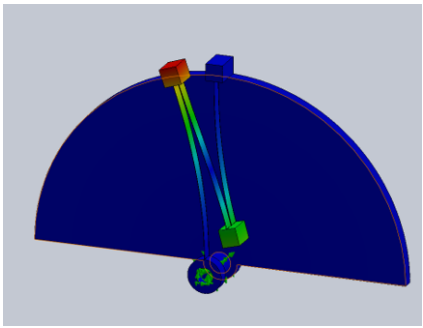
2	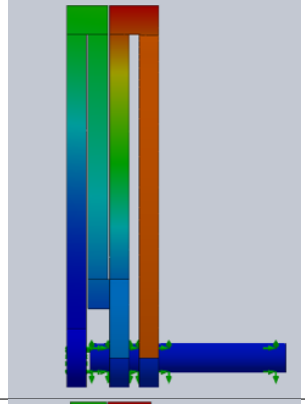	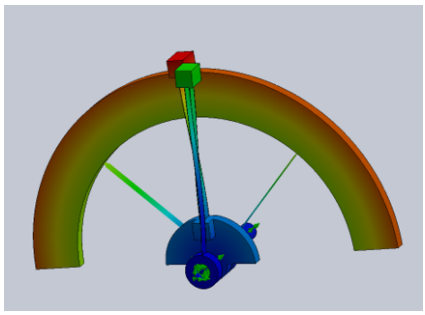	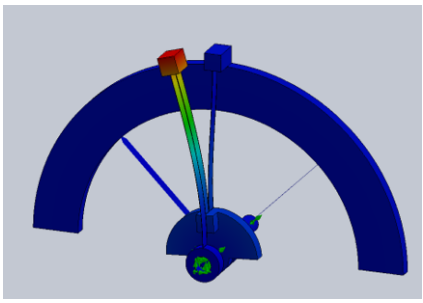
3	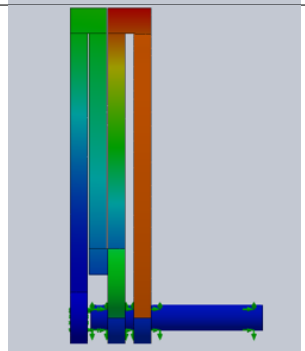	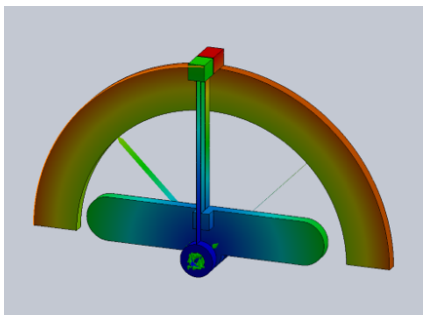	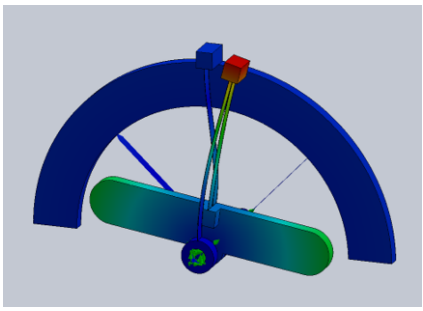
4	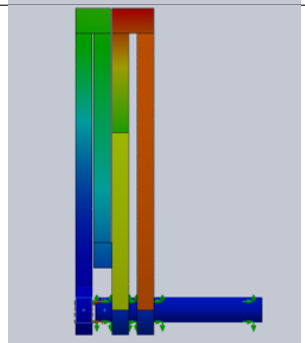	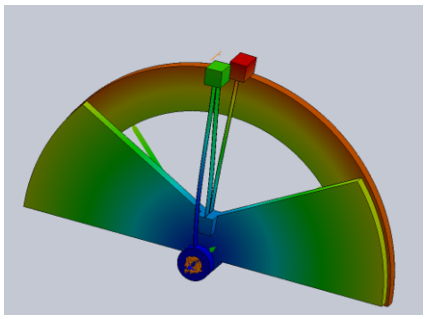	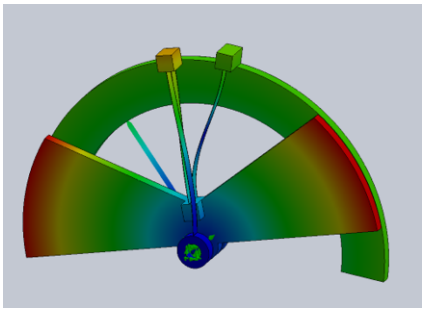
5	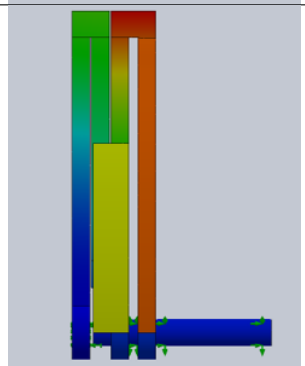	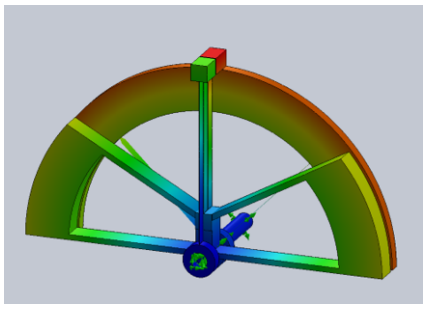	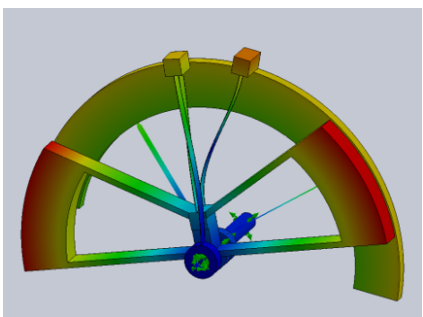

TABLE VIII: Model analysis of initial resonant designs, performed in SolidWorks.

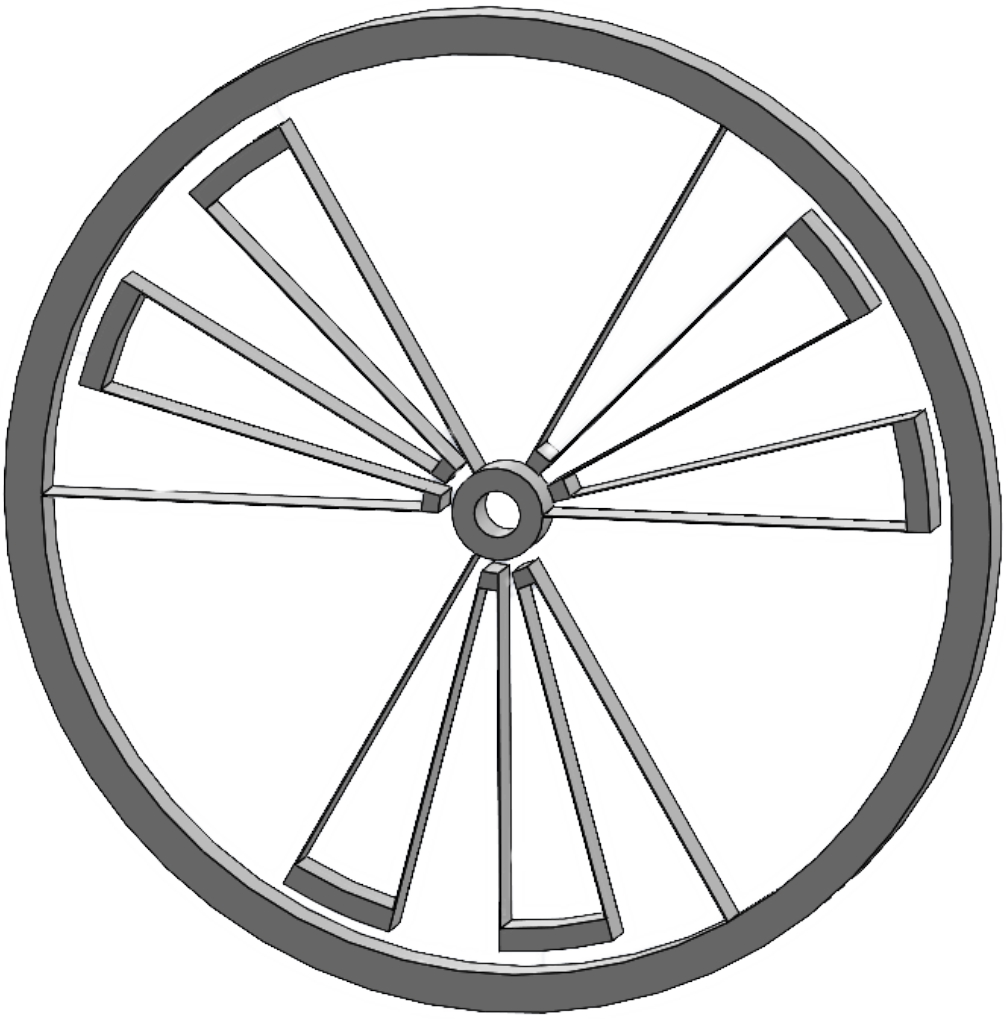

Fig. 24: A large stroke multiple leaf spring flexure mechanism proposed by Yu et al. [17]

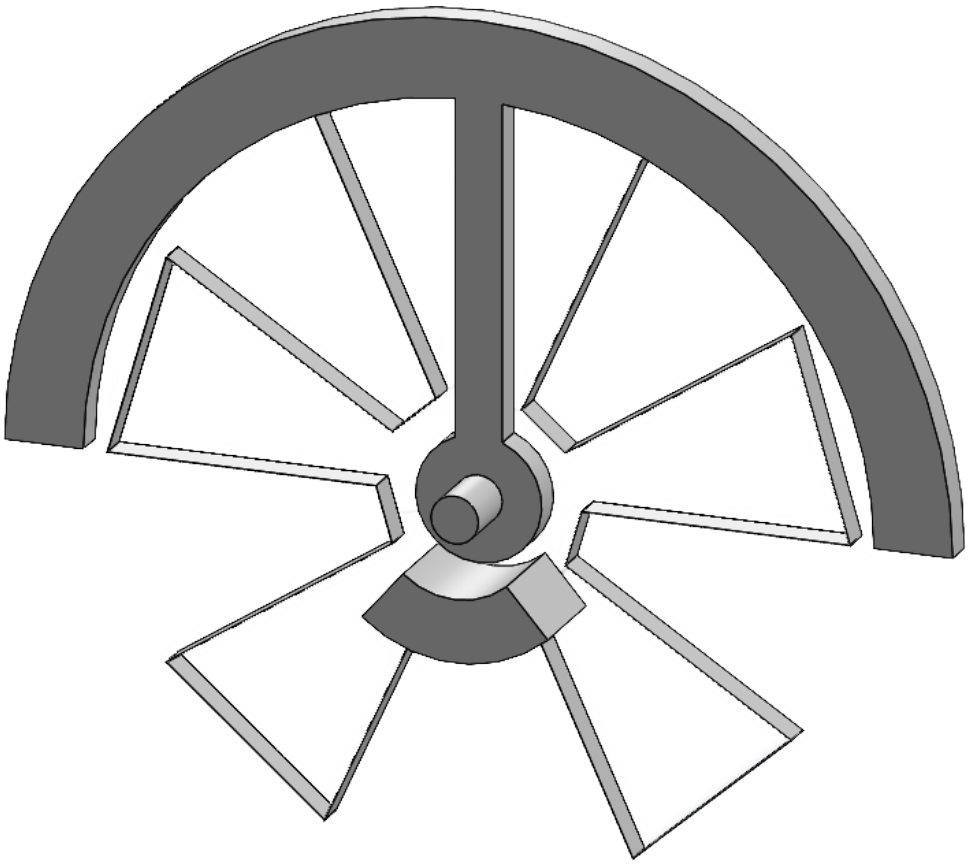

Fig. 25: The proposed sprung rotational rotor mechanism: A rotor connected to a central rotating axle, sprung by two flexures on either side connected to the ground.

Torque [Nm e-6]	**Deflection [rad]**
100	0.206
200	0.409
300	0.608
400	0.802
500	1.00
600	1.22

TABLE IX: Simulated deflection per moment load of the proposed flexure mechanism. From a finite element analysis created by Flexous.

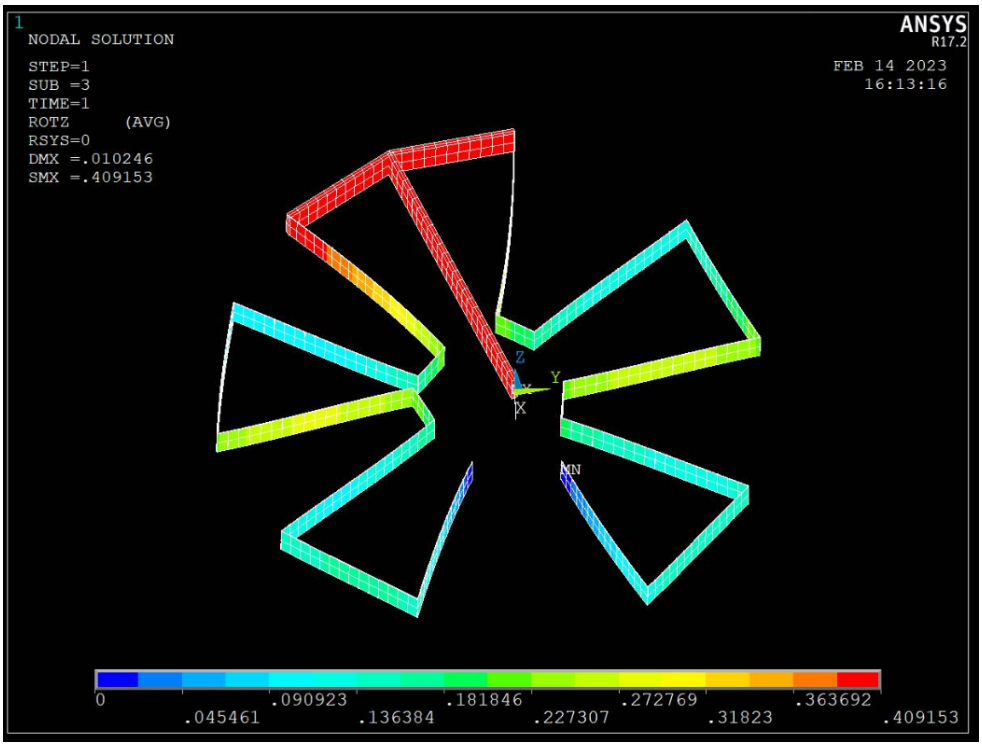

Fig. 26: Visualisation of the finite element analysis of the flexure mechanism under a moment load of 200 micro Nm.

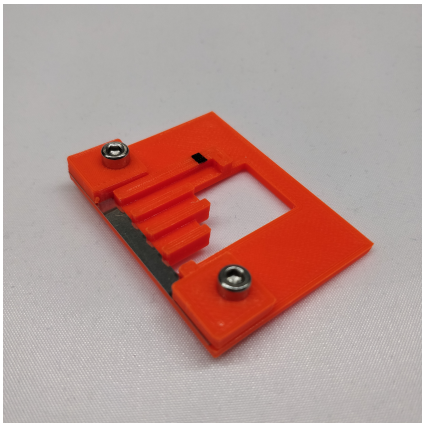

(a) Bending tool.

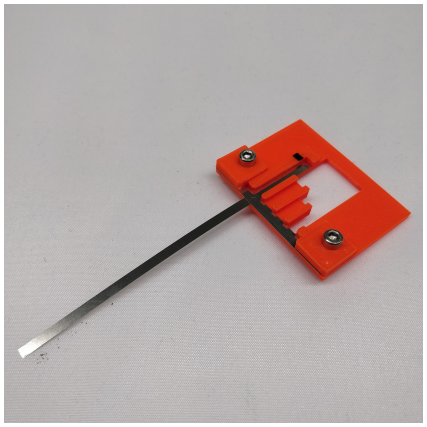

(b) Bending tool with inserted steel strip.

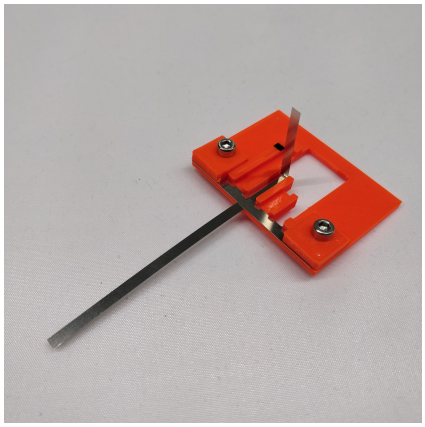

(c) Bending tool after one performed bend.

Fig. 27: Bending tool used to manufacture the flexure elements used in the proposed sprung rotational harvester.

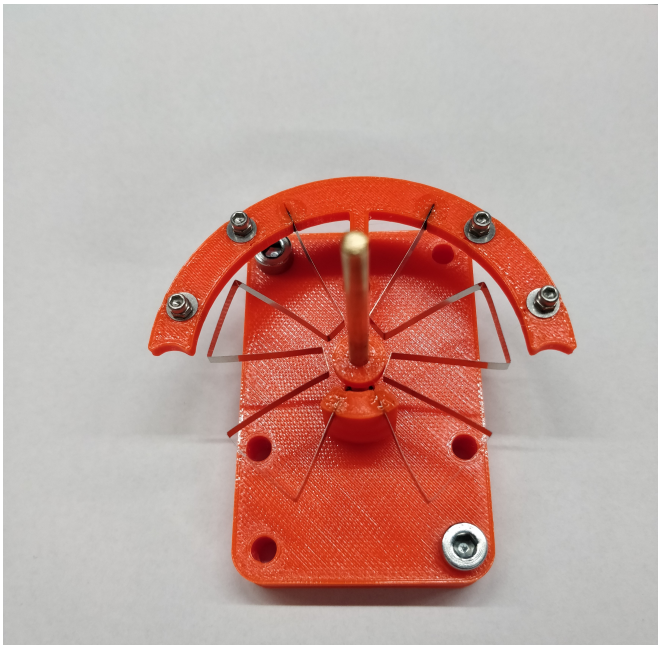

(a) Undeformed.

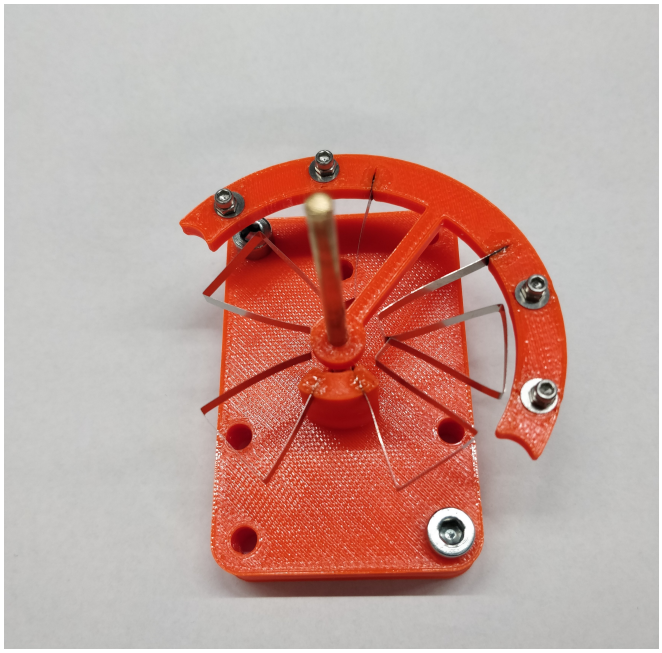

(b) Partially deformed.

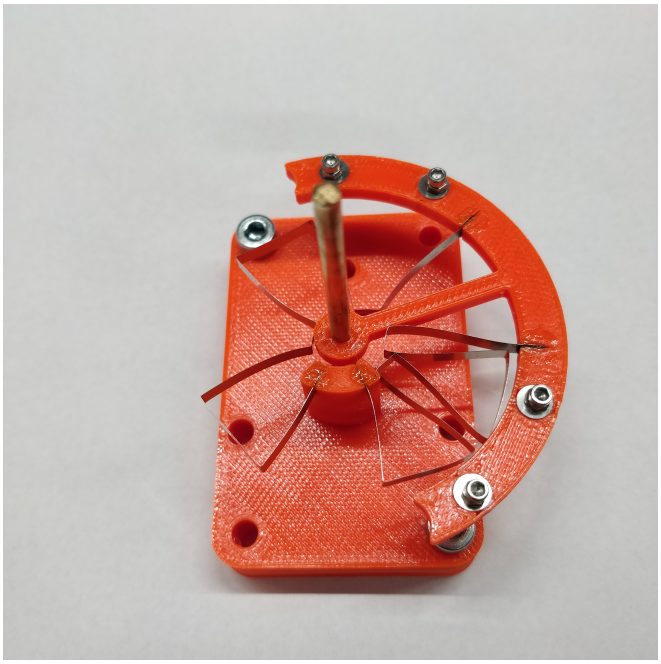

(c) Maximally deformed.

Fig. 28: The manufactured prototype flexure mechanism in undeformed and deformed position.

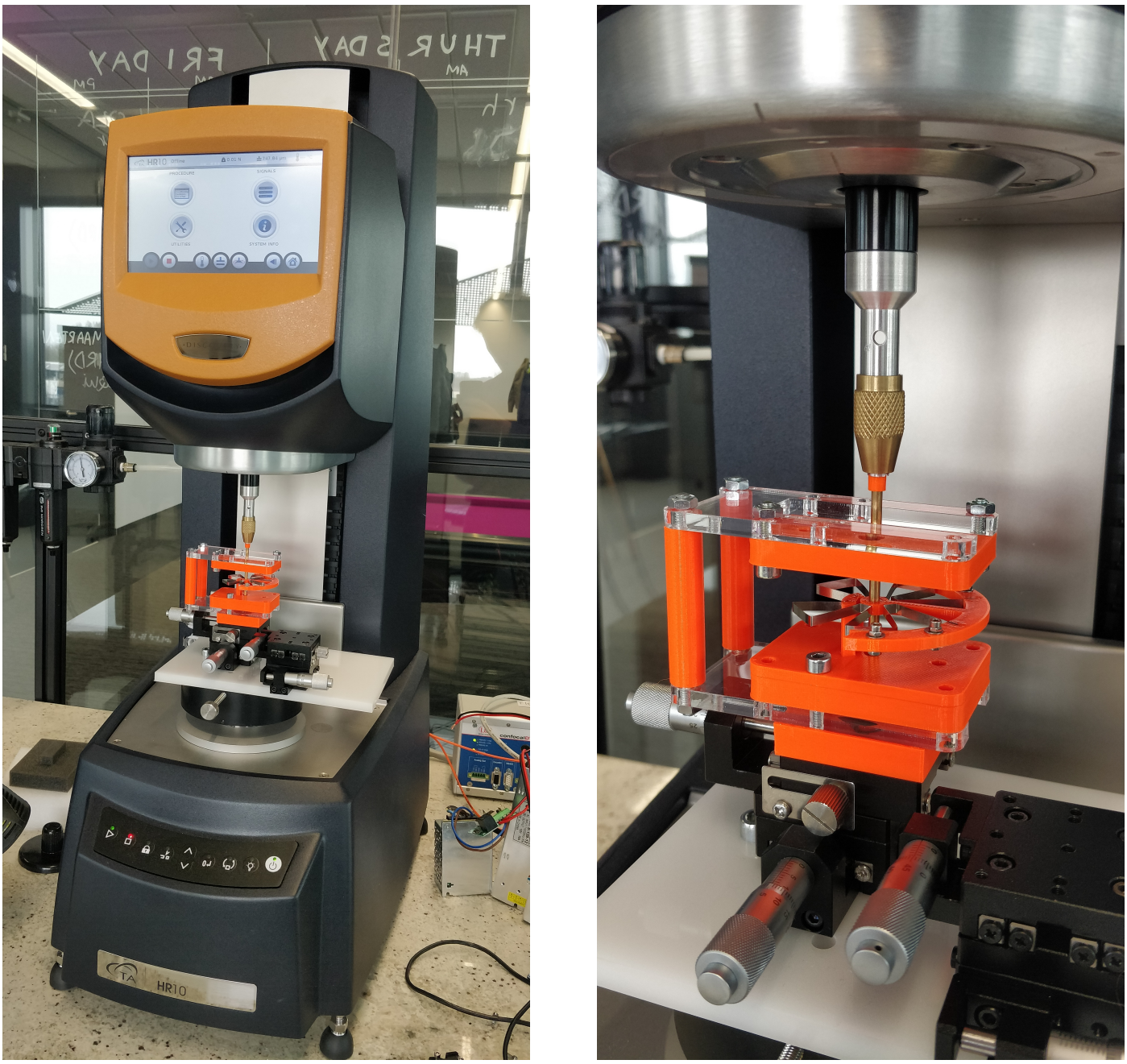

(a) Overview of the rheometer test.

(b) Detailed view of the flexure mechanism in the rheometer test.

Fig. 29: Rheometer test set-up for torque measurements of the flexure mechanism.

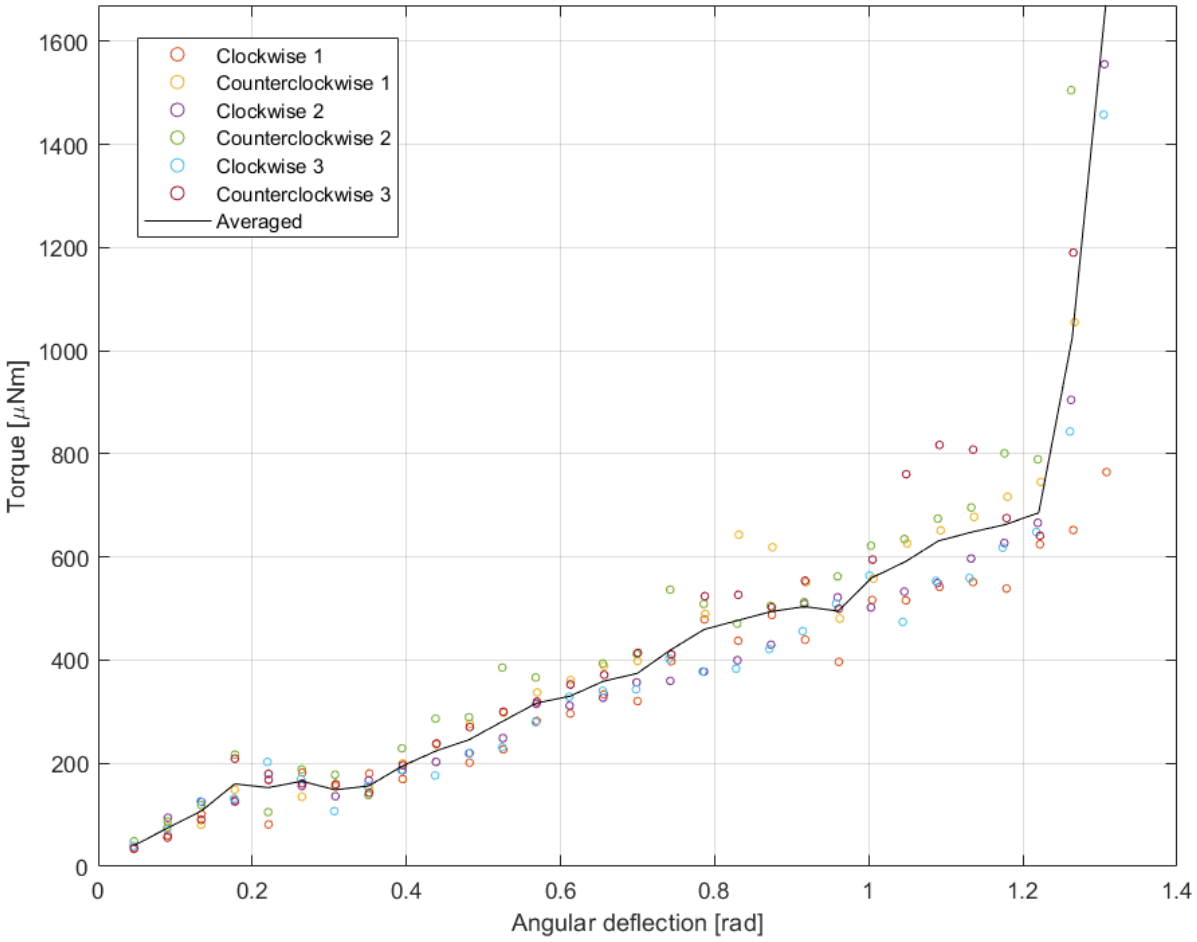

Fig. 30: Torque per deflection measurements of the flexure mechanism, performed with a rheometer.

APPENDIX D
PSEUDO WALKING TEST SET-UP

A physical pseudo walking test was created to provide a proof of concept for the flexure mechanism and to obtain an understanding of the accuracy of the simulation. The physical test was made to be similar to the simulation, arm swing amplitude and frequency could be changed and rotor angle was measured. Furthermore the angle of the arm was measured to allocate measurements to the corresponding excitation input without relying on perfect actuation of the system. Tests for both the sprung and unsprung mechanism were performed with increasing arm swing amplitudes to represent all arm swing excitations associated with walking. The sprung rotor being the previously discussed flexure mechanism and the unsprung rotor being a similar rotor without added flexure mechanism. By keeping all parameters constant and only removing the flexures the results from both tests could be compared. A schematic overview of the test set-up can be found in Fig. 32. Furthermore a schematic overview of the circuitry of the test set-up can be found in Fig. 33.

A. Actuation

The arm was actuated using a NEMA 34 stepper motor (Fig. 31a) with a maximum torque of 8.1 Nm. The motor was driven by a DS1078 Stepper Motor Driver from LAM Technologies (Fig. 31b) which was controlled by an Arduino UNO. DC power was delivered to the system by a WEHO S-100-48 switching power supply (Fig. 31c). The AccelStepper.h Arduino library was used to write a control program which was uploaded to the Arduino UNO. Arm swing amplitude and frequency were defined after which the program set a target velocity per step based on elapsed time. By deriving the desired velocity from elapsed time the sine output is independent of loop time of the Arduino UNO. The Arduino IDE code can be found at the end of Appendix D. For parts of the Arduino IDE code Chat GPT was used to have quick access to commands from the AccelStepper.h library.

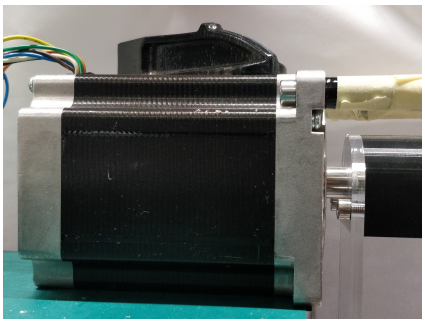

(a) NEMA 34 stepper motor used for actuation of the arm.

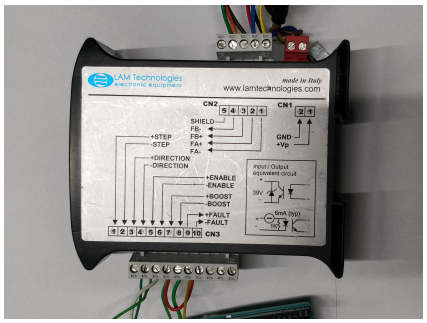

(b) LAM Technologies DS1078 Stepper Motor Driver to control the stepper motor.

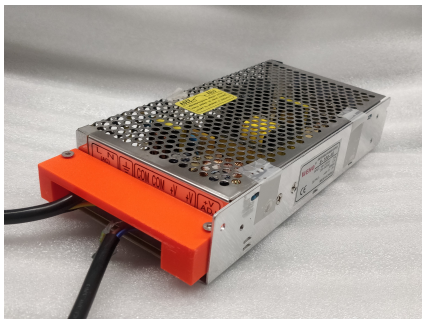

(c) WEHO S-100-48 switching power supply used to provide power.

Fig. 31: Components used for actuation of the pseudo walking test.

B. Sensing

Both the angle of the arm and the angle of the rotor axis were measured using an ams AS5600 10-bit magnetic rotary position sensor (Fig. 34a). The AS5600 senses the position of a diametrically magnetised magnet which is mounted onto the centre of rotation of the arm and the rotor axle (Fig. 34b). Both sensors were fed with 5V power and grounded using a second Arduino UNO mounted on the arm. The analog output signal of both encoders was read out using the analog input pins A1 and A2 on the Arduino UNO. The sensor gives an output between 0 and 5 Volts with a resolution of 1024 steps. A code was written and uploaded to the Arduino UNO which programmed it to send both sensor values simultaneously with a baud rate of 9600. The relative angle of both sensors with regards to the initial measurement was defined as serial output. Matlab was used to directly read out the data send from the Arduino UNO over the COM3 port of a PC. Tests were performed for 50 seconds of which the final 30 seconds were considered to be dynamically developed without significant influence from initial conditions. Data was recorded and saved in at a predefined directory. Both the Arduino IDE and Matlab code can be found at the end of Appendix D. Some parts of the Matlab and Arduino IDE code are written with the help of Chat GPT.

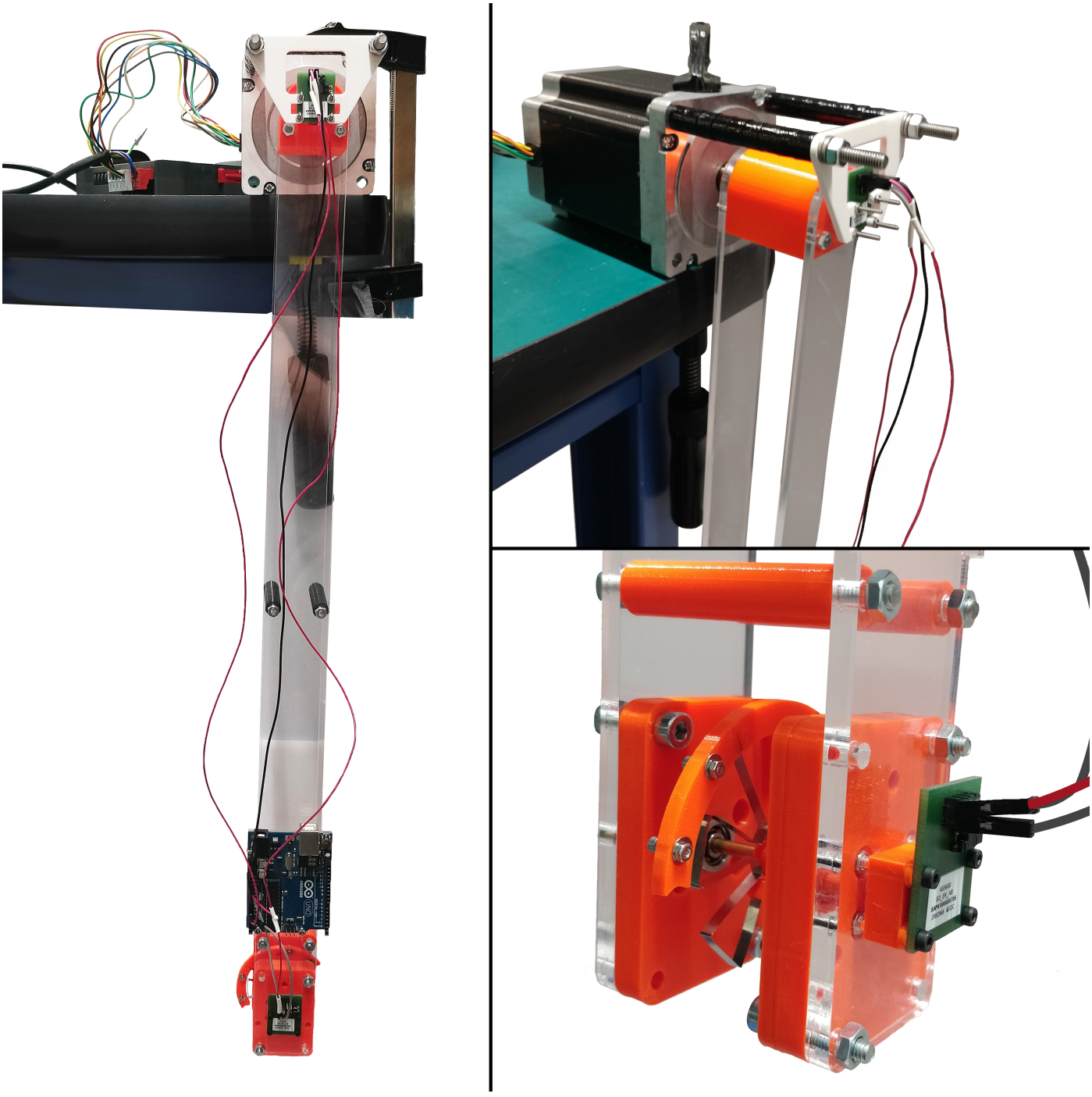

Fig. 32: Overview of the pseudo walking test set-up with detailed view of the actuation and the flexure mechanism.

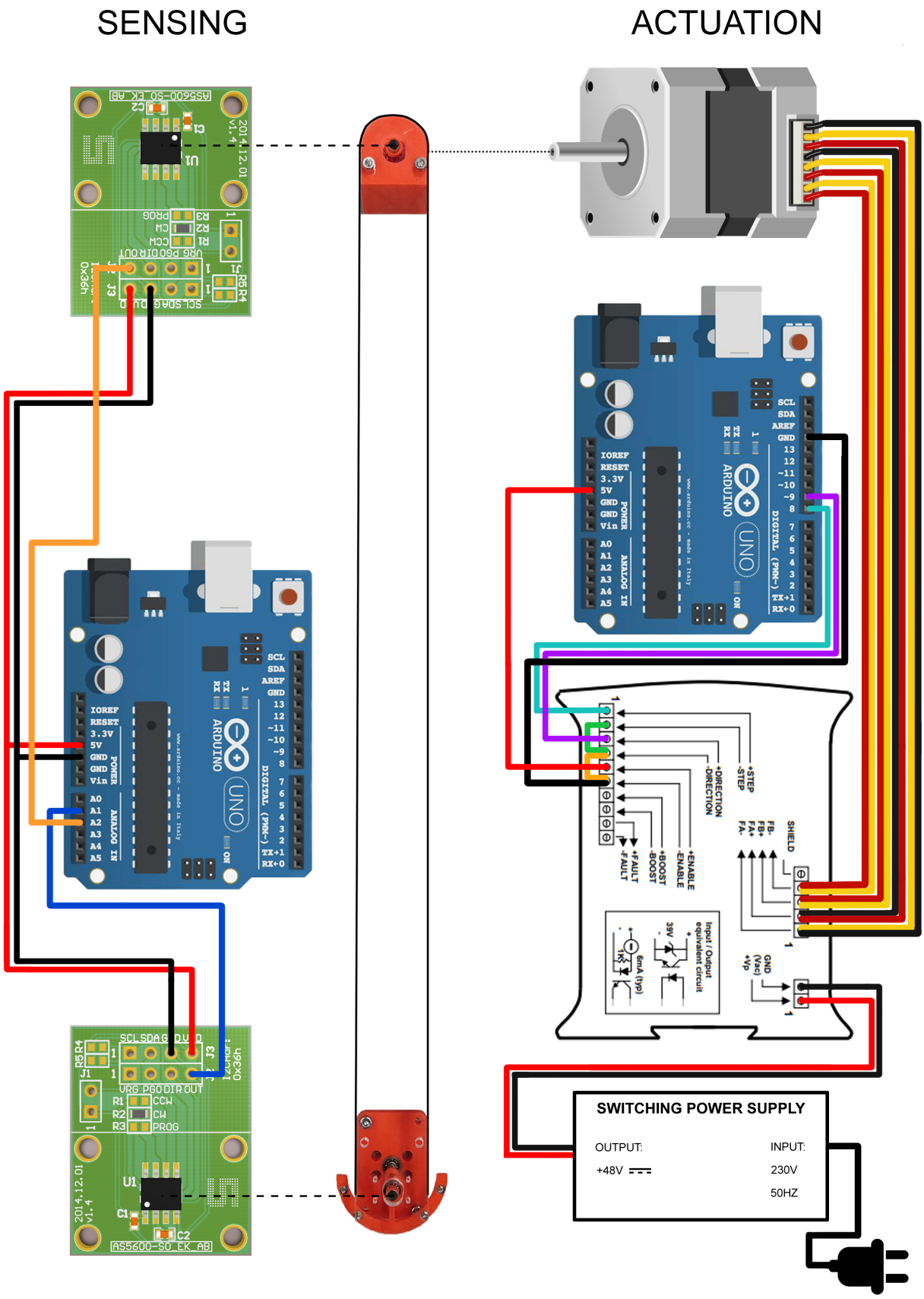

Fig. 33: Schematic overview of the pseudo walking test set-up. Showing the arm with connected rotor, two arduino UNOs, two rotary encoders, a power supply, a stepper motor and a stepper motor driver. All connections between components are shown except for the connection of both arduino UNOs to a laptop.

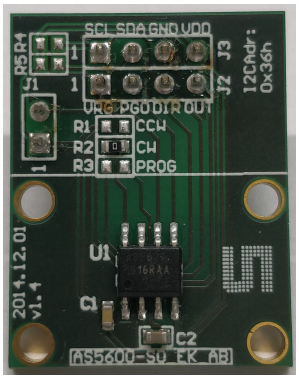

(a) ams AS5600 rotary position sensor mounted on a SO_EK_AB adapter board.

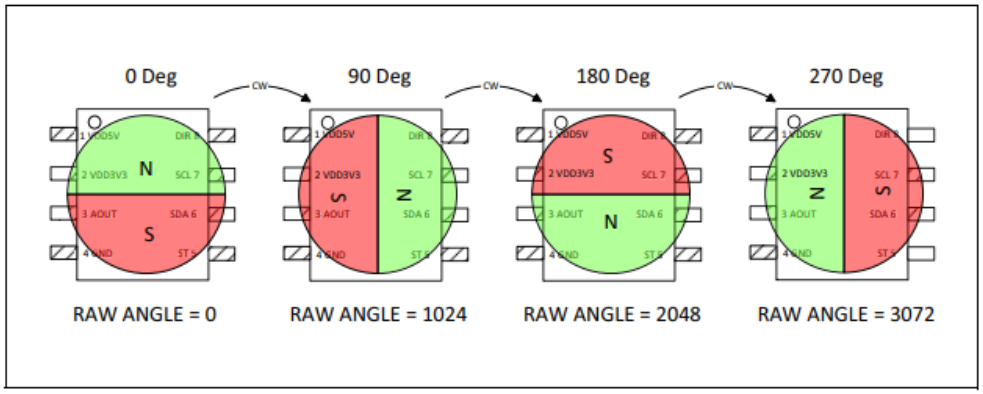

(b) Sensor readout of the AS5600 from a diametrical magnet, from the ams AS5600 datasheet.

Fig. 34: AS5600 rotary position sensor.

C. Measurement results

To account for jumps in the data caused by measurement errors a cubic smoothing spline with a smoothing parameter of 0.1 was used to filter the data. Fig. 35 shows both unfiltered and filtered measurement data of an arbitrary peak in the arm swing angle for a test at 0.9 hertz arm swing frequency and 20 degree arm swing amplitude.

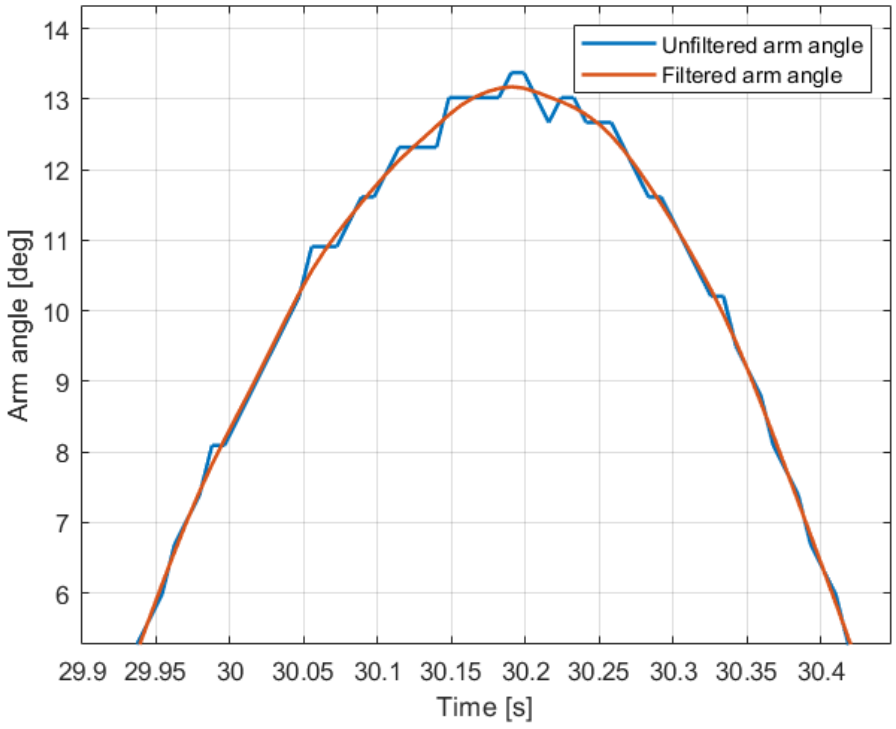

Fig. 35: Unfiltered and filtered measurements of the pseudo walking arm swing angle.

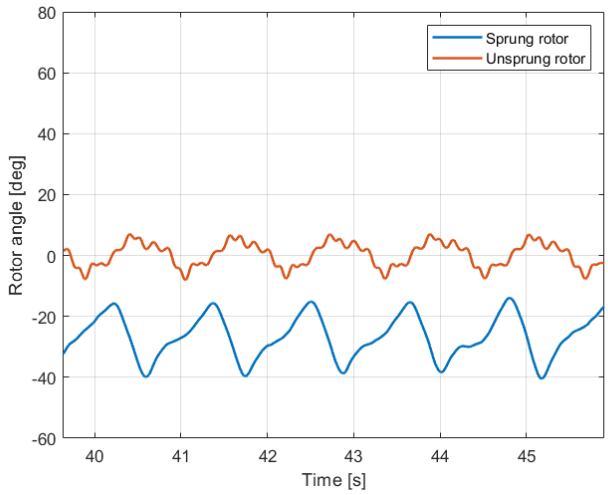

(a) 5 degree arm swing amplitude.

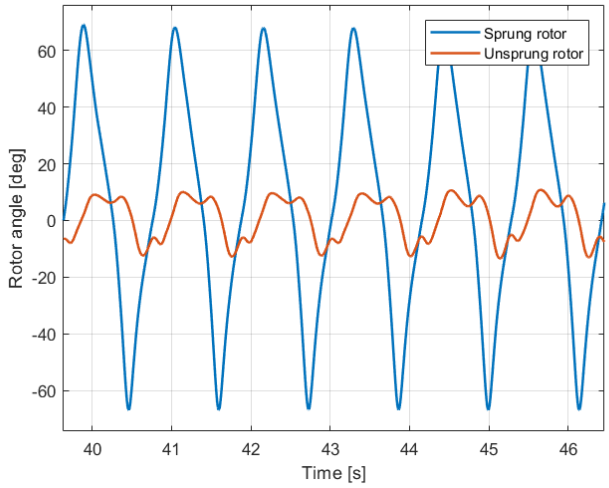

(b) 10 degree arm swing amplitude.

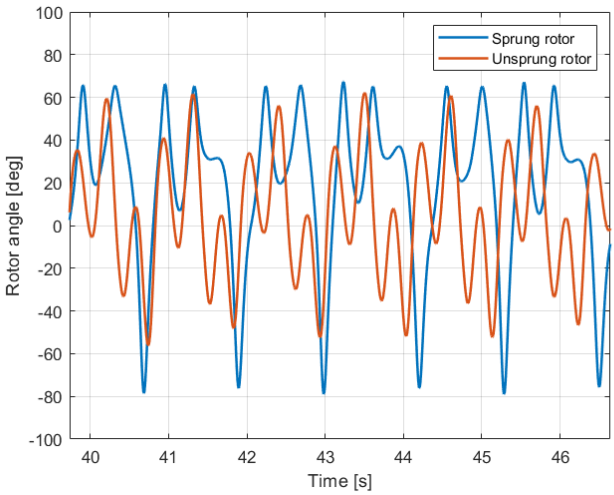

(c) 22 degree arm swing amplitude.

Fig. 36: Measurements of the rotor angle for the sprung and unsprung pseudo walking test at 0.9 Hertz arm swing frequency and 5, 10 and 22 degree arm swing amplitude. Note that, because the excitation input is not high enough at 5 degree arm swing amplitude the rotor hangs to one side.

D. Stepper control Arduino IDE code

```
#include <AccelStepper.h>

AccelStepper Stepper(1,8,9);

float t;
float A;
float B;
float Amplitude;
float Frequency;
float step;
float scale;
int Wait = 5;
#define pi 3.14159265358979323846264338327 95

void setup() {
  Stepper.setMaxSpeed(40000);
  // Stepper.setSpeed(1000);
  Stepper.setAcceleration(100);
  Serial.begin(9600);

  delay(5000);

  Amplitude = 36.32;
  Frequency = 0.9;
  step = 6400/360;
  scale = ((((2/1.68)-(2/1.8))/10)*Amplitude)+(2/1.80);

  A = (Amplitude*pi*Frequency*step*scale);
  B = (1000/(2*pi))*(1/Frequency);
}

void loop() {

 t = millis();

 if (t < 10000){
 Stepper.moveTo(-(Amplitude/2)*(100/5.2));
 Stepper.run();

 // Serial.println((Amplitude/2)*(100/5.2));
 // Serial.println(scale);
 }

 else {
 Stepper.setSpeed(A*sin(t/B));
 Stepper.runSpeed();
 // Serial.println(A*sin(t/B));
 }
}
```

E. Sensor set-up Arduino IDE code

```
#define ANALOG_PIN_1 1  // Analog pin to read from
#define ANALOG_PIN_2 2  // Analog pin to read from

int analogValue1;  // Stores the current analog value from sensor 0
int analogValue2;  // Stores the current analog value from sensor 2
int zeroPoint1;    // Stores the zero point for sensor 0
int zeroPoint2;    // Stores the zero point for sensor 2

void setup() {
  // Set the analog pins as inputs
  pinMode(ANALOG_PIN_1, INPUT);
  pinMode(ANALOG_PIN_2, INPUT);

  // Initialize the serial port for debugging
  Serial.begin(9600);
}

void loop() {
  // Read the analog signals
  analogValue1 = analogRead(ANALOG_PIN_1);
  analogValue2 = analogRead(ANALOG_PIN_2);
  // If this is the first reading for sensor 0, set the zero point
  if (zeroPoint1 == 0) {
    zeroPoint1 = analogValue1;
  }
  // If this is the first reading for sensor 2, set the zero point
  if (zeroPoint2 == 0) {
    zeroPoint2 = analogValue2;
  }
  // Calculate the relative position of the analog signals
  int position1 = analogValue1 - zeroPoint1;
  int position2 = analogValue2 - zeroPoint2;

  // Print the positions to the serial port
  Serial.print(position1);
  Serial.print(" ");
  Serial.println(position2);

}
```

F. Sensor readout Matlab code

```
clear all
close all

delete(instrfind({'Port'},{'COM3'}));

% Create a serial port object
port = serial('COM3');

% Set the baud rate and other properties of the port
set(port, 'BaudRate', 9600);
set(port, 'DataBits', 8);
set(port, 'StopBits', 1);
set(port, 'Parity', 'none');
```

```
% Open the port
fopen(port);

% Initialize the Angle1 and Angle2 arrays
Angle1 = [];
Angle2 = [];

% Start a timer
runtime = 50;

tic;

% Run the loop until runtime has elapsed
while toc < runtime
    % Read the data from the port
    data = fscanf(port);

    % Split the data into separate values
    values = strsplit(data);

    % Convert the values to numbers
    angle1 = str2double(values{1});
    angle2 = str2double(values{2});

    % Add the angles to the arrays
    Angle1 = [Angle1 angle1];
    Angle2 = [Angle2 angle2];

    % Display the data
    disp([angle1 angle2]);
end

% Close the port
fclose(port);

% Initialize the Angle1Stitched and Angle2Stitched arrays
Angle1Stitched = Angle1;
Angle2Stitched = Angle2;

% Set the threshold for detecting a jump
jumpThreshold = 300;  % Adjust this value as needed

% Loop through the angles and check for jumps
for i = 2:length(Angle1)
    % Check if Angle1 has a jump
    if abs(Angle1(i) - Angle1(i-1)) > jumpThreshold
        % Calculate the number of degrees to add or subtract to "stitch" the jump
        stitchAmount = abs(Angle1(i) - Angle1(i-1));
        % Add or subtract the calculated amount to all subsequent values of Angle1
        if Angle1(i) > Angle1(i-1)
            Angle1Stitched(i:end) = Angle1Stitched(i:end) - stitchAmount;
        else
            Angle1Stitched(i:end) = Angle1Stitched(i:end) + stitchAmount;
        end
    end
    % Check if Angle2 has a jump
    if abs(Angle2(i) - Angle2(i-1)) > jumpThreshold
```

```
        % Calculate the number of degrees to add or subtract to "stitch" the jump
        stitchAmount = abs(Angle2(i) - Angle2(i-1));
        % Add or subtract the calculated amount to all subsequent values of Angle2
        if Angle2(i) > Angle2(i-1)
            Angle2Stitched(i:end) = Angle2Stitched(i:end) - stitchAmount;
        else
            Angle2Stitched(i:end) = Angle2Stitched(i:end) + stitchAmount;
        end
    end
end


% Use csaps to smooth the Angle1 data
Angle1Filtered = csaps(1:length(Angle1Stitched), Angle1Stitched, 0.1);
Angle2Filtered = csaps(1:length(Angle2Stitched), Angle2Stitched, 0.1);

Angle1Filtered = ppval(Angle1Filtered, 1:length(Angle1));
Angle2Filtered = ppval(Angle2Filtered, 1:length(Angle2));

% Create a matrix to store the mapped values
AngleMap = zeros(length(Angle1), 4);

% Map the values in Angle1 and Angle2 to degrees
for i = 1:length(Angle1)
    AngleMap(i,1) = (Angle1Stitched(i) / 1023) * 360;
    AngleMap(i,2) = (Angle2Stitched(i) / 1023) * 360;
    AngleMap(i,3) = (Angle1Filtered(i) / 1023) * 360;
    AngleMap(i,4) = (Angle2Filtered(i) / 1023) * 360;
end

% Get the time values for each sample
time = linspace(0, runtime, length(Angle1));

% Set the file name and path
filename = 'Unsprung_0.9Hz_36.32Deg.mat';
filepath = 'C:\Users\Sam van den Oever\Desktop\HTE\Afstuderen\Experiment\Results\
   Flexure 1\Pseudo walking\Unsprung\';  % Change this to the desired path

% Save the data to the filex
save([filepath filename], 'AngleMap', 'time');

% Plot the angles against time
figure;
plot(time, AngleMap(:,1), '-g');
hold on;
plot(time, AngleMap(:,2), '-y');
hold on
plot(time, AngleMap(:,3), '-r');
hold on
plot(time, AngleMap(:,4), '-b');
xlabel('Time (seconds)');
ylabel('Angle (degrees)');
legend('Angle 1', 'Angle 2');
```

APPENDIX E
FURTHER RESEARCH

Further research should be performed to investigate the implementation of the proposed flexure mechanism into an off-the-shelf wearable energy harvester. Scaling of the flexures and testing under actual wrist movement are the main points of interest. After the test results of the pseudo-walking test presented in this research were processed, Flexous started a parallel investigation of exactly this scalability and implementability by creating a silicon flexure at scale and integrating it into an ETA watch movement. The flexure mechanism was successfully manufactured out of silicon and initial tests showed the flexure's capability to introduce a rotational stiffness to existing harvester movements. Other further research could be done to expand the simulation model by incorporating a more realistic walking motion based on data from accelerometers worn during walking.